
LILAN: A LINEAR LATENT NETWORK APPROACH FOR REAL-TIME SOLUTIONS TO STIFF NONLINEAR ORDINARY DIFFERENTIAL EQUATIONS

William Cole Nockolds

Oden Institute for Computational Engineering and Sciences,
University of Texas at Austin
Austin, TX 78712
cole.nockolds@utexas.edu

C G Krishnanunni

Dept of Aerospace Engineering & Engineering Mechanics,
University of Texas at Austin
Austin, TX 78712
krishnanunni@utexas.edu

Tan Bui-Thanh

Oden Institute for Computational Engineering and Sciences,
Dept of Aerospace Engineering & Engineering Mechanics,
University of Texas at Austin
Austin, TX 78712
tanbui@oden.utexas.edu

Xianzhu Tang

Theoretical Division, Los Alamos National Laboratory
Los Alamos, NM 87545, United States of America
xtang@lanl.gov

ABSTRACT

Solving stiff ordinary differential equations (StODEs) requires sophisticated numerical solvers, which are often computationally expensive. In general, traditional explicit time integration schemes with restricted time step sizes are not suitable for StODEs, and one must resort to costly implicit methods to compute solutions. On the other hand, state-of-the-art machine learning (ML) based methods such as Neural ODE (NODE) poorly handle the timescale separation of various elements of the solutions to StODEs, while still requiring expensive implicit/explicit integration at inference time. In this work, we propose a linear latent network (LiLaN) approach in which the dynamics in the latent space can be integrated analytically, and thus numerical integration is completely avoided. At the heart of LiLaN are the following key ideas: i) two encoder networks to encode initial condition together with

parameters of the ODE to the slope and the initial condition for the latent dynamics, respectively. Since the latent dynamics, by design, are linear, the solution can be evaluated analytically; ii) a neural network to map the initial condition, parameters, and the physical time to latent times, one for each latent variable. Intuitively, this allows for the "stretching/squeezing" of time in the latent space, thereby allowing for varying levels of attention to different temporal scales in the solution. Finally, iii) a decoder network to decode the latent solutions into the physical solution at the corresponding physical time. *LiLaN is thus a solution operator approach that instantly provides an approximate flow map solution of a system of nonlinear ODEs at any time.* We provide a universal approximation theorem for the proposed LiLaN approach, showing that it can approximate the solution of any stiff nonlinear system on a compact set to any degree of accuracy ε . We also show an interesting fact that the dimension of the latent dynamical system in LiLaN is independent of ε . Numerical results on "Robertson Stiff Chemical Kinetics Model" [1] and "Plasma Collisional-Radiative Model" [2] suggest that LiLaN outperformed state-of-the-art machine learning approaches for handling StODEs. Numerically, we also show that LiLaN outperformed other machine learning methods on multiple partial differential equations (PDEs) with known stiff behaviors, such as the "Allen-Cahn" and "Cahn-Hilliard" PDEs [3].

Keywords

stiff ordinary differential equations; Stiff partial differential equations; Latent dynamics; Encoder-decoder architecture

1 Introduction

Stiff ordinary differential equations (StODEs), arising in many scientific and engineering disciplines, pose unique challenges for numerical integration. While a precise definition of stiffness has eluded mathematicians for decades, systems characterized by numerical stiffness typically have important behaviors on timescales that differ by several orders of magnitude. In order to realize these features and ensure that the solution remains bounded during numerical integration with explicit methods, extremely small time steps must be taken [4], making explicit integration prohibitively expensive. It has been established that stiff problems are generally solved more efficiently using implicit methods, which are more costly at each integration step, than with explicit methods [5]. Stiff solvers often require solving a nonlinear system of equations at each integration step [5] which drastically increases the computational requirements for large systems. For certain applications, specifically for control, design, optimization, and uncertainty quantification scenarios, one often needs to run an expensive forward model many times [6], which renders implicit approaches computationally infeasible. The expensive nature of solving StODEs, whether by explicit or implicit numerical methods, necessitates the development of novel machine learning (ML) techniques for accelerating simulation of such systems.

In recent years, scientific machine learning techniques have been deployed as a faster alternative to traditional numerical solvers [1, 7, 8, 9, 10]. One popular approach for modeling dynamical systems is the Neural ODE (NODE) approach, which approximates the right-hand side of an ordinary differential equation (ODE) using a neural network [11, 12]. However, as discussed in [13], NODE struggles to learn solutions of stiff systems of ODEs. The authors propose scaling factors, derived from the data, which can be used to normalize the NODE dynamics such that learning stiff dynamical systems becomes feasible [13]. Specifically, the scaling factors help balance the scales of different components in the loss function to make training less challenging for the optimizer. Furthermore, it was shown that, for stiff problems, the implementation of explicit conservation of mass constraints in the loss function during NODE training led to significantly better performance than an unconstrained NODE approach [14]. Another NODE-based approach considers encoding the ODE system to a latent space and implements an explicit constraint in the loss function to minimize an estimate of the stiffness ratio for the latent dynamics, showing promising results on two reaction equations [10]. These modifications to vanilla NODE exhibited great success in the simulation of stiff ODEs. However, though NODE-based

approaches were able to achieve reasonable accuracy on stiff problems, all of the methods discussed still require the use of an expensive, implicit integrator at inference time.

Another approach, the physics-informed neural network (PINN), described in [15], has received significant attention for its ability to speed up the simulation of ODEs and PDEs. Training a PINN results in a function that can be evaluated to approximate the solution of an ODE/PDE, and thus avoids expensive numerical integration entirely. However, it was shown in [16] that the gradient flow dynamics for training PINNs are typically stiff themselves, placing strict limitations on the gradient descent step size required for stable training. Stiff gradient dynamics may mean that gradient descent cannot effectively optimize network parameters during training and the optimization may diverge [16]. One solution to this problem is proposed in [17], which illustrates a method utilizing quasi-steady state assumptions (QSSA) to convert a stiff system into one that is non-stiff and thus easier for PINNs to handle. The work in [18] proposed a different, but effective solution to the problem of learning stiff ODEs, using PINNs, by augmenting the loss function with conservation of energy constraints and implementing a sequential training process which prioritizes learning the early temporal evolution of the ODE during early epochs and gradually increasing the time interval seen in training. Additionally, in [19], the authors were able to accurately simulate stiff ODEs using a modified PINN architecture based on solving the corresponding integral form of the ODE of interest. The aforementioned approaches showed significant improvements in accuracy over the basic PINN architecture, which typically struggles to learn solutions for stiff ODEs. While the PINN approach is efficient due to avoiding numerical integration, and the modifications to the PINN approach described in [17, 18, 19] have allowed PINNs to model stiff problems more accurately than before, PINNs have their own issues, such as not being generalizable to unseen initial and boundary conditions, unless retraining is carried out.

Several approaches to simulate dynamical systems involve the use of autoencoders to learn a latent dynamical system, typically of lower dimensionality than the original system, that is faster to solve than the original model. The latent solutions are then decoded to approximate solutions using trained decoders [9, 10, 20, 21, 22, 23, 24]. The encoders and decoders can be trained to handle a wide range of initial conditions, boundary conditions, and input parameters so that the latent dynamical system holds significant information about the true dynamics under many different circumstances. However, without a good estimate of the intrinsic dimensionality of the system, important information could be lost in the encoding process [25]. On the other hand, some new approaches propose increasing the dimension of the state through nonlinear featurization. In the area of reservoir computing, methods that utilize high-dimensional "reservoir" representations of data have shown promise in the integration of stiff and even chaotic systems [1, 7, 26]. Additionally, in the reinforcement learning (RL) community, augmenting the state vector with nonlinear featurization has been shown to improve the training of RL algorithms for certain tasks [27]. Even though these reservoir computing approaches increase the dimensionality of the original problem, they achieve speedup at inference time because they do not require classical numerical integration at inference time (such as in the case for NODE). Instead, the result of training is a neural network that can be evaluated to obtain the solution to the stiff system at the desired future time. The approach we will propose in this paper follows this philosophy, i.e., expanding the dimension of the problem through nonlinear featurization to approximate solution operators—i.e., the flow map—of the stiff ODE without requiring numerical integration.

While the approaches we have discussed above have shown some speedup in integration, while still accurately predicting the solutions to StODEs, major challenges remain. In the NODE approaches, for example, while [10, 13, 14] demonstrate the ability of NODE to learn stiff dynamics, each approach still necessitates the use of an expensive implicit solver at inference time. On the other hand, while the PINN approaches [17, 18, 19] do not require expensive implicit integration, they must be retrained for new boundary and/or initial conditions. The QSSA approach [17] works by removing the fastest evolving components of the solution, meaning that the information about those components will be lost, though that information is important for many applications such as those in this paper. Similarly, the approach in [1], though it obtained significant speedup results, can be inaccurate due to exhibiting oscillatory behavior, resembling Gibb's phenomenon, in prediction. Other work that presented speedup results showed only mild speedup and often only under specific test conditions [7, 10]. In [9], multiple orders of magnitude of speedup were achieved; however, the

approach presented lacks any theoretical guarantees. In this work, we will propose an approach which not only provides an approximate solution operator to achieve a remarkable speedup, but also maintains a high level of accuracy when evaluated across a wide range of new initial conditions and parameter inputs, even for the fastest evolving components of the solution to stiff systems.

In particular, we developed an autoencoder-based approach, called LiLaN (Linear Latent Network), to accelerate the simulation of StODEs by approximating the solution operator (i.e., the flow map in the context of ODEs). LiLaN is inspired by kernel methods, in which the original problem under consideration is featurized/lifted to (much) higher-dimensional feature spaces where the problem is now easier. In particular, a similar intuition is that, given a stiff dynamical system, it may be possible to learn a non-stiff, higher-dimensional latent dynamical system with trivial solutions. Unlike kernel methods, which rely on particular feature maps to organize the latent dynamics so that hopefully it is easier to simulate, LiLaN forces the latent dynamics to be trivially linear, and then learns the nonlinear feature maps using neural networks. To achieve this goal, we deploy an encoder that takes in the initial condition of the original dynamical system as input and outputs the initial condition for the latent dynamics. Furthermore, by implicitly imposing a constant velocity latent dynamics structure, we completely evade numerical integration in the latent space since the solution is a sequence of fully linear trajectories and can therefore be computed analytically. The trained decoder can then retrieve, from the latent representation, the solution to the original dynamics, at any desirable time. Our theoretical analysis reveals that under mild assumptions, one can approximate the flow map of a stiff, nonlinear system on a compact set to any degree of accuracy, ε , using LiLaN, and that the required dimension of the latent space is independent of ε . Additionally, our theoretical results mandate that employing a nonlinear transformation on the time variable is necessary to guarantee that a LiLaN architecture exists which can approximate a given flow map. Intuitively, this transformation allows for "stretching/squeezing" time in the latent space, thereby allowing for varying levels of attention to different temporal regions of the solution. Numerical experiments on the "Robertson Stiff Chemical Kinetics Model" [1] and the "Plasma Collisional-Radiative Model" [2] suggest that LiLaN can outperform state-of-the-art ML approaches for calculating solutions to StODEs. Additionally, LiLaN outperformed other machine learning methods on multiple PDEs with known stiff behaviors, such as the "Allen-Cahn" and "Cahn-Hilliard" PDEs [3]. It should be pointed out that though we focus on stiff ODEs, LiLaN is equally applicable to non-stiff ODEs.

2 Mathematical framework

In this work, all the vectors are represented in boldface small, and matrices are represented in boldface capital. We consider the following autonomous parametrized StODE:

$$\frac{d\mathbf{x}}{dt} = \mathbf{f}(\mathbf{x}, \mathbf{p}), \quad \mathbf{x}(0) = \mathbf{x}_0, \quad (1)$$

where $\mathbf{f}(\mathbf{x}, \mathbf{p}) : \mathcal{G} \times \mathcal{X}_p \rightarrow \mathbb{R}^{n_x}$, with $\mathcal{G} \subseteq \mathbb{R}^{n_x}$ denoting a non-empty open set, and $\mathcal{X}_p \subset \mathbb{R}^{n_p}$ denoting a non-empty, compact set, and $\mathbf{x}_0 \in \mathcal{G}$. Here, \mathbf{p} is the n_p dimensional parameter vector which does not vary with time and $\mathbf{x}(t)$ is the n_x dimensional state vector.

Definition 1 (Flow map) By \mathcal{W} we denote the following

$$\mathcal{W} = \bigcup_{\mathbf{x}_0 \in \mathcal{G}, \mathbf{p} \in \mathcal{X}_p} I_{\mathbf{x}_0; \mathbf{p}} \times \{\mathbf{x}_0\} \times \{\mathbf{p}\} \subseteq \mathbb{R} \times \mathcal{G} \times \mathcal{X}_p,$$

where $I_{\mathbf{x}_0; \mathbf{p}}$ is the maximal interval of existence of the solution¹ of (1) for a given \mathbf{x}_0, \mathbf{p} . We define the flow map (if it exists) to be the function $\psi : \mathcal{W} \rightarrow \mathcal{G}$ such that $\psi(t, \mathbf{x}_0, \mathbf{p}) = \mathbf{x}(t)$, where $\mathbf{x}(t)$ is a solution of (1) at time t for a given $\{\mathbf{x}_0, \mathbf{p}\}$.

¹Refer to [28] for the definition of maximal interval of existence of the solution.

The objective in this work is to develop a surrogate model for approximating the solution $\mathbf{x}(t)$, and thus the flow map, on some closed and bounded interval I , for any given $\mathbf{p} \in \mathcal{X}_p$, $\mathbf{x}_0 \in \mathcal{G}$ (assuming that $I \subseteq I_{\mathbf{x}_0, \mathbf{p}}$ for all \mathbf{p} , \mathbf{x}_0).

2.1 Description of the proposed LiLaN approach

In this section, we present the key components of LiLaN. LiLaN deploys four neural networks:

- **Encoders $e(\mathbf{x}_0, \mathbf{p}; \beta)$ and $c(\mathbf{x}_0, \mathbf{p}; \alpha)$** : Note that both e and c are neural networks with parameters β and α respectively. The network $e(\cdot, \cdot, \beta) : \mathcal{G} \times \mathcal{X}_p \mapsto \mathbb{R}^m$ takes in \mathbf{x}_0, \mathbf{p} , as defined in (1), as inputs and outputs an m dimensional initial condition for the latent dynamical system given below:

$$\text{diag} \left(\frac{d\mathbf{y}}{d\tau} \right) = \mathbf{c}(\mathbf{x}_0, \mathbf{p}; \alpha), \quad \mathbf{y}(\mathbf{0}) = e(\mathbf{x}_0, \mathbf{p}; \beta) = \mathbf{y}_0, \quad (2)$$

where $\text{diag} \left(\frac{d\mathbf{y}}{d\tau} \right)$ extracts the diagonal elements of matrix $\left[\frac{d\mathbf{y}}{d\tau} \right]$ into a column vector, $\mathbf{y}(\tau) \in \mathbb{R}^m$ denotes the solution to (2) given by (3), $\tau \in \mathbb{R}^m$ is a nonlinear transformation of time as described by a neural network below. The network $c(\cdot, \cdot, \alpha) : \mathcal{G} \times \mathcal{X}_p \mapsto \mathbb{R}^m$ takes in \mathbf{x}_0, \mathbf{p} , as defined in (1), as inputs and outputs an m dimensional slope vector (constant velocity) for the latent dynamics as described in (2).

- **Nonlinear Time Transformation $\tau(t, \mathbf{x}_0, \mathbf{p}; \nu)$** : In (2), τ is a neural network with parameters ν . The network $\tau(\cdot, \cdot, \cdot, \nu) : I \times \mathcal{G} \times \mathcal{X}_p \mapsto \mathbb{R}^m$ performs a nonlinear transformation on the time variable which "stretches/squeezes" time in the latent space, thereby allowing for varying levels of attention to different regions/dynamics in the solution depending on the inputs \mathbf{x}_0, \mathbf{p} . Note that the solution of (2) is a sequence of linear trajectories,

$$\mathbf{y}(\tau) = e(\mathbf{x}_0, \mathbf{p}; \beta) + \tau \circ \mathbf{c}(\mathbf{x}_0, \mathbf{p}; \alpha), \quad (3)$$

where \circ denotes the Hadamard product for vectors.

- **Decoder $d(\mathbf{y}; \theta)$** : The decoder network $d(\cdot; \theta) : \mathbb{R}^m \mapsto \mathbb{R}^{n_x}$ with parameters, θ , decodes the solution, \mathbf{y} , in (3), back to the solution of original dynamics, \mathbf{x} , in (1).

Based on the above networks, our procedure can be summarized as follows. For a given initial condition, \mathbf{x}_0 , and parameters, \mathbf{p} , the encoders, e and c generate the initial condition and the constant velocity vector for the latent dynamics described in (2). The solution of this latent dynamics at a latent time τ is given in (3). The decoder then retrieves the solution $\mathbf{x}(t)$ to the original dynamics (1). The networks are trained, in tandem, to find the optimal parameters $\alpha, \beta, \theta, \nu$ that minimize the loss function (details in Section A.2) that compares the generated solution $\hat{\mathbf{x}}(t)$ to the true solution $\mathbf{x}(t)$. The training data for LiLaN take the form:

$$\{\{\mathbf{x}_0, \mathbf{p}\}_i, \{\mathbf{x}(t_0), \mathbf{x}(t_1), \dots, \mathbf{x}(t_M)\}_i\}_{i=1}^N, \quad (4)$$

where N is the total number of training sample trajectories, and t_0, \dots, t_M are the temporal collocation points for each trajectory, which are used to construct the loss function (see Section A.2 for more details).

It should be noted that an independent approach² by Sulzer and Buck [9] considers a fully linear latent space to simulate stiff dynamics. Even though the method lacks theoretical guarantees, it achieves multiple orders of magnitude of speedup versus a traditional numerical solver. Here we highlight key differences between LiLaN and the method proposed by Sulzer and Buck [9]. Notably, their method does not consider a learned nonlinear transformation on the time variable, denoted by τ in this work. The authors also emphasize the use of a lower-dimensional latent space (i.e., $m < n_x$) in their approach. Additionally, they assumed that the parameters \mathbf{p} are fixed-i.e., \mathbf{p} in (1) remains constant across all training samples. The objective then is to train a surrogate model to simulate the trajectory $\mathbf{x}(t)$ for new unseen initial conditions \mathbf{x}_0 in (1). The latent NODE in their approach, analogous to our c , takes as input the latent

²We were not aware of their work during the development of LiLaN. Our inspiration is kernel methods as discussed at the end of section 1.

initial condition \mathbf{y}_0 rather than the true initial condition \mathbf{x}_0 . In section 3, we provide extensive numerical experiments comparing the performance of LiLaN with the approach by Sulzer and Buck [9]. Specifically, we evaluate two variants of their method: i) Sulzer and Buck I: Their original approach with a reduced latent dimension (i.e. $m \leq n_x$); and ii) Sulzer and Buck II: Their approach with an expanded latent dimension (i.e. $m \geq n_x$).

2.2 The LiLaN approach

2.2.1 "Direct learning" is a special case of LiLaN

When dealing with stiff systems, integration using both implicit and explicit methods can be computationally expensive. If the flow map is continuous on a compact set, then by the universal approximation theorem for neural networks [29, 30], theoretically, one could use a single hidden layer neural network to learn the flow map to any degree of accuracy, ε . That is, there exists a one-hidden layer neural network that can predict the future state of the system for any given initial condition, parameters, and future time. In particular, denoting the flow map in definition 1 as $\psi(t, \mathbf{x}_0, \mathbf{p}) = \psi(\mathbf{z})$ (where $\mathbf{z} = (t, \mathbf{x}_0, \mathbf{p})$), and the universal neural network as

$$\mathcal{N}_{\text{direct}}(\mathbf{z}) = \mathbf{W}_1 \phi(\mathbf{W}\mathbf{z} + \mathbf{b}) + \mathbf{c}_1, \quad (5)$$

where $\mathbf{W}_1 \in \mathbb{R}^{n_x \times m}$, $\mathbf{W} \in \mathbb{R}^{m \times (1+n_x+n_p)}$, $\mathbf{b} \in \mathbb{R}^m$, $\mathbf{c}_1 \in \mathbb{R}^{n_x}$ denotes the weights and biases of the network $\mathcal{N}_{\text{direct}}$, ϕ is a nonlinear activation function, and m denotes the number of neurons in the hidden layer. Note that in this approach, the neural network (5) tries to learn the ground truth flow map $\psi(\mathbf{z})$ based on the training data 4. This procedure completely avoids numerical integration at inference time and provides an extremely fast surrogate model. We call this approach the "**direct learning**" approach.

We now show that "**direct learning**" is a special case of our proposed LiLaN approach in section 2.1. To that end, note that the direct neural network in (5) can be equivalently written as:

$$\mathcal{N}_{\text{direct}}(t, \mathbf{x}_0, \mathbf{p}) = \mathbf{W}_1 \phi(\mathbf{W}_t t + \mathbf{W}_{\mathbf{x}_0} \mathbf{x}_0 + \mathbf{W}_{\mathbf{p}} \mathbf{p} + \mathbf{b}) + \mathbf{c}_1, \quad (6)$$

where $\mathbf{W}_t \in \mathbb{R}^{m \times 1}$ denotes the first column of \mathbf{W} , $\mathbf{W}_{\mathbf{x}_0} \in \mathbb{R}^{m \times n_x}$ denotes the 2^{nd} to $(n_x + 1)^{th}$ columns of \mathbf{W} , $\mathbf{W}_{\mathbf{p}} \in \mathbb{R}^{m \times n_p}$ denotes the $(n_x + 2)^{th}$ to $(n_x + n_p + 1)^{th}$ columns of \mathbf{W} . Next, by choosing

$$\begin{aligned} e(\mathbf{x}_0, \mathbf{p}; \{\mathbf{W}_{\mathbf{x}_0}, \mathbf{W}_{\mathbf{p}}, \mathbf{b}\}) &= \mathbf{W}_{\mathbf{x}_0} \mathbf{x}_0 + \mathbf{W}_{\mathbf{p}} \mathbf{p} + \mathbf{b}, \quad \mathbf{c}(\mathbf{x}_0, \mathbf{p}) = \mathbf{1}_m, \quad \tau(t, \mathbf{x}_0, \mathbf{p}; \mathbf{W}_t) = \mathbf{W}_t t, \\ \mathbf{d}(\mathbf{y}; \{\mathbf{W}_1, \mathbf{c}_1\}) &= \mathbf{W}_1 \phi(\mathbf{y}) + \mathbf{c}_1, \end{aligned} \quad (7)$$

then the LiLaN approach in section 2.1 reduces to eq. (6).

Remark 1

1. Note that instead of employing simple linear encoders and linear time transformation as in eq. (7), LiLaN deploys deep nonlinear encoders $e(\mathbf{x}_0, \mathbf{p}; \beta)$ and $\mathbf{c}(\mathbf{x}_0, \mathbf{p}; \alpha)$, and a deep nonlinear time transformation network $\tau(t, \mathbf{x}_0, \mathbf{p}; \nu)$. This is expected to improve the expressiveness of networks, possibly requiring significantly fewer parameters to learn the flow map [31, 32]. In Figure 1, we demonstrate how employing nonlinear encoders and time transformation improves the generalization performance of the architecture. Figure 1 (left) depicts the average point-wise relative error of predictions (see (42)) over time for the test dataset from section 3.2.2, with LiLaN, shown in blue, and the "**direct learning**" approach shown in orange. LiLaN greatly outperforms the "**direct learning**" approach, having at least an order of magnitude lower error than the direct learning approach for the majority of the simulation time interval. Both methods become less accurate in the middle portion of the trajectory, where the dynamics for the collisional-radiative cooling model (section 3.2.2) begin evolving on very small timescales. However, the "**direct learning**" approach, struggles more in this region, shown by the larger increase in error. The error of the direct learning approach decreases to a similar value to that of LiLaN as the dynamics approach steady state near $t = 10^{-3}$ s. Viewing

figure 1 (right), we observe that while both approaches reached very low final losses on the training data, the "direct learning" approach failed to generalize to unseen cases as well, signified by the larger validation loss, which did not converge. Note that, for a fair comparison, both approaches were given approximately the same number of learnable parameters and the same data-points for training.

2. In section 2.2.2 we will present a universal approximation theorem for LiLaN, which also provides a new proof of the universal approximation theorem for the direct approach as a by-product.

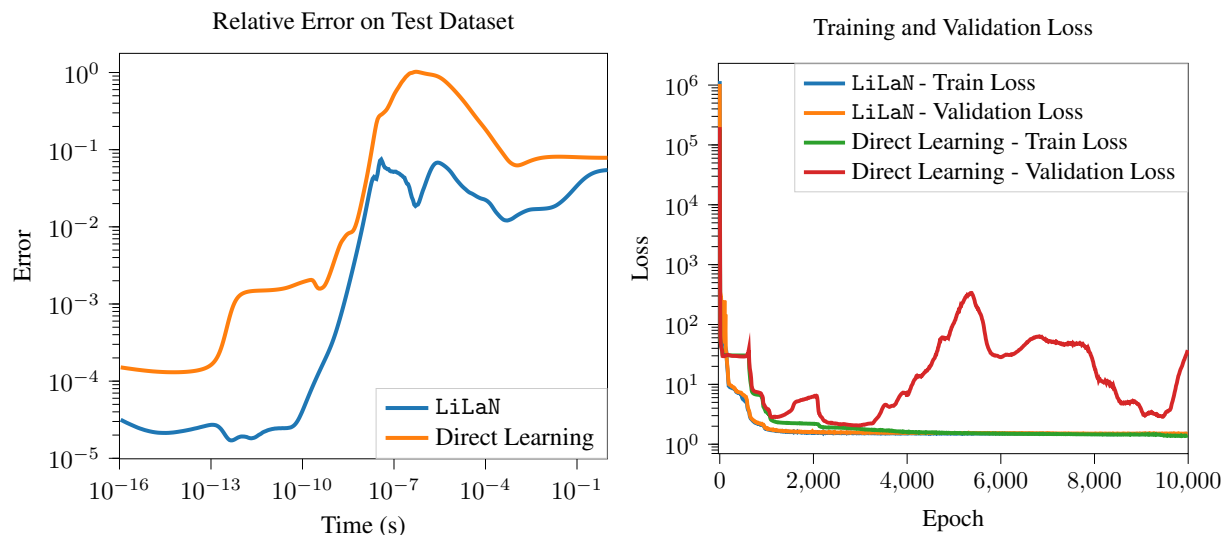


Figure 1: Learning flow map by LiLaN, vs. "direct learning" approach. Left to Right: Average point-wise relative error (42) in predictions for the full CR model (section 3.2) on the test dataset, depicting LiLaN having at least an order of magnitude lower error for the majority of the simulation; Training and validation loss curves for the two approaches. These curves demonstrate that validation loss of the "direct learning" approach fails to converge, while LiLaN validation loss remains very close to the training loss.

2.2.2 Universal approximation for LiLaN

In the following sections, we will prove a universal approximation theorem for LiLaN presented in section 2.1. We begin with a definition.

Definition 2 (Class of functions $\mathcal{N}_{a,b}^\phi$) Let $\phi : \mathbb{R} \rightarrow \mathbb{R}$ be any non-affine, Lipschitz continuous function which is continuously differentiable at least at one point, having a nonzero derivative at that point. We denote by $\mathcal{N}_{a,b}^\phi$ the class of functions described by feedforward neural networks with 'a' neurons in the input layer, 'b' neurons in the output layer, and an arbitrary number of hidden layers, each with 'a + b + 2' neurons and activation function ϕ . Every neuron in the output layer has the identity activation function.

Remark 2 Note that commonly employed activation functions in deep learning such as 'Tanh', 'Sigmoid', 'ReLU', and 'ELU' satisfy the conditions in definition 2.

We will start by examining the conditions on $\mathbf{f}(\mathbf{x}(t), \mathbf{p})$ such that for any given \mathbf{x}_0 , \mathbf{p} the solution exists on the entire real line and the flow map is continuous with respect to its arguments. The result is summarized in lemma 1.

Lemma 1 Consider the autonomous ordinary differential equation in (1). Assume that $\mathbf{f}(\mathbf{x}(t), \mathbf{p})$ is globally Lipschitz continuous with respect to both $\mathbf{x}(t)$ and \mathbf{p} ³. Then, the flow map in definition 1, $\psi(t, \mathbf{x}_0, \mathbf{p})$, is continuous on \mathcal{W} with $I_{\mathbf{x}_0; \mathbf{p}} = \mathbb{R}$.

Proof: Rewriting the ODE (1) in terms of a new variable $\tilde{\mathbf{x}}(t)$ as:

$$\frac{d\tilde{\mathbf{x}}}{dt} = \tilde{\mathbf{f}}(\tilde{\mathbf{x}}(t)), \quad \tilde{\mathbf{x}}(t) = \begin{bmatrix} \mathbf{x}(t) \\ \mathbf{p} \end{bmatrix}, \quad \tilde{\mathbf{x}}(0) = \tilde{\mathbf{x}}_0 = \begin{bmatrix} \mathbf{x}_0 \\ \mathbf{p} \end{bmatrix}, \quad (8)$$

where

$$\tilde{\mathbf{f}}(\tilde{\mathbf{x}}(t)) = \begin{bmatrix} \mathbf{f}(I_1 \tilde{\mathbf{x}}(t), I_2 \tilde{\mathbf{x}}(t)) \\ \mathbf{0} \end{bmatrix}.$$

where, I_1 projects $\tilde{\mathbf{x}}(t)$ to $\mathbf{x}(t)$, and I_2 projects $\tilde{\mathbf{x}}(t)$ to \mathbf{p} , and they are linear and differentiable. Since $\mathbf{f}(\mathbf{x}, \mathbf{p})$ is globally Lipschitz continuous, by the global existence theorem (Theorem B, Chapter 13 in [33]), we note that \mathbb{R} is the interval of existence of the unique maximal solution of (8) for any given $\tilde{\mathbf{x}}_0$. Also note that $\tilde{\mathbf{f}}$ is continuous on \mathcal{P} , where $\mathcal{P} = \mathcal{G} \times \mathcal{X}_p$, due to the assumption that $\mathbf{f}(\mathbf{x}(t), \mathbf{p})$ is globally Lipschitz continuous with respect to both \mathbf{p} and $\mathbf{x}(t)$. Now introduce the set:

$$\tilde{\mathcal{W}} = \bigcup_{\tilde{\mathbf{x}}_0 \in \mathcal{P}} \mathbb{R} \times \{\tilde{\mathbf{x}}_0\} \subseteq \mathbb{R} \times \mathcal{P},$$

and define the corresponding flow map for (8) as $\psi_{\tilde{\mathbf{x}}} : \tilde{\mathcal{W}} \rightarrow \mathcal{P}$ such that $\psi_{\tilde{\mathbf{x}}}(t, \tilde{\mathbf{x}}_0) = \tilde{\mathbf{x}}(t)$, where $\tilde{\mathbf{x}}(t)$ solves (8) for a given $\tilde{\mathbf{x}}_0$. Since $\tilde{\mathbf{f}}$ is continuous on \mathcal{P} , by Theorem 6.1 in [34], we have $\psi_{\tilde{\mathbf{x}}}(t, \tilde{\mathbf{x}}_0)$ is continuous on $\tilde{\mathcal{W}}$. Now, defining $\psi(t, \mathbf{x}_0, \mathbf{p}) = \psi_{\tilde{\mathbf{x}}}(t, \tilde{\mathbf{x}}_0)$ concludes the proof.

Proposition 1 There exists a continuous function $\mathbf{l}(\mathbf{y}) : \mathbb{R}^{n_x} \mapsto \mathbb{R}^m$ ($m \geq n_x$) with a continuous left-inverse $\mathbf{l}^{-1}(\mathbf{z}) : \text{Range}(\mathbf{l}) \mapsto \mathbb{R}^{n_x}$.

Proof: We prove the assertion by constructing a function with the desirable properties. In this proof, the exponential and logarithm are Hadamard exponential and logarithm, that is, with a given vector input, both exponential and logarithm act in a componentwise fashion. Now, consider the functions $\mathbf{l}(\mathbf{y}) : \mathbb{R}^{n_x} \mapsto \mathbb{R}^m$ and $\mathbf{g}(\mathbf{z}) : \text{Range}(\mathbf{l}) \mapsto \mathbb{R}^{n_x}$ as follows:

$$\mathbf{l}(\mathbf{y}) = \log(\mathbf{1} + e^{\mathbf{A}\mathbf{y}}), \quad \mathbf{l}^{-1}(\mathbf{z}) = \mathbf{A}^\dagger(\log(e^{\mathbf{z}} - \mathbf{1})), \quad (9)$$

where $\mathbf{A} \in \mathbb{R}^{m \times n_x}$ ($m \geq n_x$) is an arbitrary matrix with linearly independent columns, and $\mathbf{A}^\dagger \in \mathbb{R}^{n_x \times m}$ is the pseudo-inverse of \mathbf{A} . Clearly $\mathbf{g}(\mathbf{z})$ is a left-inverse of $\mathbf{l}(\mathbf{y})$ and both are continuous functions on \mathbb{R}^{n_x} and $\text{Range}(\mathbf{l})$, respectively.

Next, we will determine the conditions under which the flow map admits the following decomposition:

$$\psi(t, \mathbf{x}_0, \mathbf{p}) = \mathbf{l}^{-1}(\mathbf{g}(\mathbf{x}_0, \mathbf{p}) + \mathbf{h}(t, \mathbf{x}_0, \mathbf{p}) \circ \mathbf{b}(\mathbf{x}_0, \mathbf{p})), \quad (10)$$

where a continuous function $\mathbf{l}(\mathbf{y}) : \mathbb{R}^{n_x} \mapsto \mathbb{R}^m$ and its left-inverse \mathbf{l}^{-1} are given in proposition 1, $\mathbf{g}(\mathbf{x}_0, \mathbf{p}) : \mathcal{G}_0 \times \mathcal{X}_p \mapsto \mathbb{R}^m$ continuous with respect to both arguments, $\mathbf{b}(\mathbf{x}_0, \mathbf{p}) : \mathcal{G}_0 \times \mathcal{X}_p \mapsto \mathbb{R}^m$ continuous with respect to both arguments, and $\mathbf{h}(t, \mathbf{x}_0, \mathbf{p}) : I \times \mathcal{G}_0 \times \mathcal{X}_p \mapsto \mathbb{R}^m$ continuous with respect to all arguments. Here, I is a closed and bounded interval, $\mathbf{x}_0 \in \mathcal{G}_0 \subset \mathcal{G}$ is a given non-empty compact set. The result is summarized in lemma 2.

Lemma 2 Consider the autonomous ordinary differential equation in (1) and assume the following:

1. The conditions in lemma 1 are satisfied.

³ $\mathbf{f}(\mathbf{x}, \mathbf{p})$ is globally Lipschitz continuous if there exists a non-negative constant M such that $\|\mathbf{f}(\mathbf{x}_1, \mathbf{p}_1) - \mathbf{f}(\mathbf{x}_2, \mathbf{p}_2)\|_2 \leq M \|\mathbf{r}_1 - \mathbf{r}_2\|_2, \forall \mathbf{r}_1, \mathbf{r}_2 \in \mathbb{R}^{n_x + n_p}$, where $\mathbf{r}_1 = [\mathbf{x}_1, \mathbf{p}_1]$ and $\mathbf{r}_2 = [\mathbf{x}_2, \mathbf{p}_2]$.

2. Assume that the initial condition $\mathbf{x}_0 \in \mathcal{G}_0 \subset \mathcal{G}$, where \mathcal{G}_0 is a non-empty compact set, and consider a set $E = I \times \mathcal{G}_0 \times \mathcal{X}_p$, where $I = [0, t^u]$, with $t^u \in \mathbb{R}^+$, is a closed and bounded interval.

Then, there exists a (non-unique⁴) decomposition for a given flow map ψ as follows:

$$\psi(t, \mathbf{x}_0, \mathbf{p}) = \mathbf{l}^{-1}(\mathbf{g}(\mathbf{x}_0, \mathbf{p}) + \mathbf{h}(t, \mathbf{x}_0, \mathbf{p}) \circ \mathbf{b}(\mathbf{x}_0, \mathbf{p})), \quad (11)$$

where the functions \mathbf{l} , \mathbf{b} , \mathbf{g} , \mathbf{h} have the following properties:

- $\mathbf{l}(\mathbf{y}) : \mathbb{R}^{n_x} \mapsto \mathbb{R}^m$ ($m \geq n_x$) belongs to the space of continuous functions with a continuous left-inverse denoted as $\mathbf{l}^{-1}(\mathbf{z}) : \text{Range}(\mathbf{l}) \mapsto \mathbb{R}^{n_x}$ ⁵;
- $\mathbf{b}(\mathbf{x}_0, \mathbf{p}) : \mathcal{G}_0 \times \mathcal{X}_p \mapsto \mathbb{R}^m$ belongs to the space of strictly non-zero continuous functions on $\mathcal{G}_0 \times \mathcal{X}_p$;
- $\mathbf{g}(\mathbf{x}_0, \mathbf{p}) : \mathcal{G}_0 \times \mathcal{X}_p \mapsto \mathbb{R}^m$ belongs to the space of continuous functions on $\mathcal{G}_0 \times \mathcal{X}_p$, and $\mathbf{h}(t, \mathbf{x}_0, \mathbf{p}) : I \times \mathcal{G}_0 \times \mathcal{X}_p \mapsto \mathbb{R}^m$ belong to the space of continuous functions on $I \times \mathcal{G}_0 \times \mathcal{X}_p$.

Proof: Given the flow map ψ and a function \mathbf{l} let us decompose the action of \mathbf{l} on the flow map $\psi(t, \mathbf{x}_0, \mathbf{p})$ as follows:

$$\mathbf{l}(\psi(t, \mathbf{x}_0, \mathbf{p})) = \mathbf{l}(\psi(t^*, \mathbf{x}_0, \mathbf{p})) + \mathbf{u}(t, \mathbf{x}_0, \mathbf{p}), \quad (12)$$

for some $t^* > 0$ in the interval I , and the function $\mathbf{u}(t, \mathbf{x}_0, \mathbf{p})$ is defined as $\mathbf{u}(t, \mathbf{x}_0, \mathbf{p}) = \mathbf{l}(\psi(t, \mathbf{x}_0, \mathbf{p})) - \mathbf{l}(\psi(t^*, \mathbf{x}_0, \mathbf{p}))$. Note that $\psi(t^*, \mathbf{x}_0, \mathbf{p})$ exists since the solution exists on the entire real line for any $(\mathbf{x}_0, \mathbf{p}) \in \mathcal{G}_0 \times \mathcal{X}_p$ (see lemma 1). Further, $\mathbf{u}(t, \mathbf{x}_0, \mathbf{p})$ is continuous on E due to the fact the continuity of $\psi(t, \mathbf{x}_0, \mathbf{p})$ and \mathbf{l} . Now define the following functions:

$$\mathbf{g}(\mathbf{x}_0, \mathbf{p}) = \mathbf{l}(\psi(t^*, \mathbf{x}_0, \mathbf{p})),$$

$$\mathbf{h}_i(t, \mathbf{x}_0, \mathbf{p}) \mathbf{b}_i(\mathbf{x}_0, \mathbf{p}) = \mathbf{u}_i(t, \mathbf{x}_0, \mathbf{p}) = \mathbf{r}_i(\mathbf{x}_0, \mathbf{p}) \frac{\mathbf{u}_i(t, \mathbf{x}_0, \mathbf{p})}{\mathbf{r}_i(\mathbf{x}_0, \mathbf{p})},$$

where $\mathbf{r}_i(\mathbf{x}_0, \mathbf{p}) : \mathcal{G}_0 \times \mathcal{X}_p \mapsto \mathbb{R}^m$ is a strictly non-zero continuous function. Finally, by taking $\mathbf{b}_i(\mathbf{x}_0, \mathbf{p}) = \mathbf{r}_i(\mathbf{x}_0, \mathbf{p})$ and $\mathbf{h}_i(t, \mathbf{x}_0, \mathbf{p}) = \frac{\mathbf{u}_i(t, \mathbf{x}_0, \mathbf{p})}{\mathbf{r}_i(\mathbf{x}_0, \mathbf{p})}$, (12) can be rewritten as:

$$\mathbf{l}(\psi(t, \mathbf{x}_0, \mathbf{p})) = \mathbf{g}(\mathbf{x}_0, \mathbf{p}) + \mathbf{h}(t, \mathbf{x}_0, \mathbf{p}) \circ \mathbf{b}(\mathbf{x}_0, \mathbf{p}). \quad (13)$$

Now applying the left inverse \mathbf{l}^{-1} on both sides of (13) we have:

$$\begin{aligned} \mathbf{l}^{-1}(\mathbf{l}(\psi(t, \mathbf{x}_0, \mathbf{p}))) &= \mathbf{l}^{-1}(\mathbf{g}(\mathbf{x}_0, \mathbf{p}) + \mathbf{h}(t, \mathbf{x}_0, \mathbf{p}) \circ \mathbf{b}(\mathbf{x}_0, \mathbf{p})) \\ \implies \psi(t, \mathbf{x}_0, \mathbf{p}) &= \mathbf{l}^{-1}(\mathbf{g}(\mathbf{x}_0, \mathbf{p}) + \mathbf{h}(t, \mathbf{x}_0, \mathbf{p}) \circ \mathbf{b}(\mathbf{x}_0, \mathbf{p})), \end{aligned} \quad (14)$$

where we used the fact that $\mathbf{l}^{-1}(\mathbf{l}(\mathbf{y})) = \mathbf{y}$ since the left-inverse exists by assumption, and this concludes the proof.

We are now in the position to present the universal approximation theorem for LiLaN.

Theorem 1 Consider the autonomous ordinary differential equation in (1) and assume that the conditions in lemma 2 are satisfied.

Then, $\forall m \geq n_x$, m being the latent dimension, and $\forall \varepsilon > 0$, there exist four neural networks $\mathbf{d}(\cdot; \boldsymbol{\theta}) : \mathbb{R}^m \mapsto \mathbb{R}^{n_x}$, $\mathbf{e}(\cdot, \cdot; \boldsymbol{\beta}) : \mathcal{G}_0 \times \mathcal{X}_p \mapsto \mathbb{R}^m$, $\mathbf{c}(\cdot, \cdot; \boldsymbol{\alpha}) : \mathcal{G}_0 \times \mathcal{X}_p \mapsto \mathbb{R}^m$, and $\boldsymbol{\tau}(\cdot, \cdot, \cdot; \boldsymbol{\nu}) : \mathbb{R} \times \mathcal{G}_0 \times \mathcal{X}_p \mapsto \mathbb{R}^m$ with the associated latent dynamics:

$$\text{diag}\left(\frac{d\mathbf{y}}{d\boldsymbol{\tau}}\right) = \mathbf{c}(\mathbf{x}_0, \mathbf{p}; \boldsymbol{\alpha}), \quad \mathbf{y}(0) = \mathbf{e}(\mathbf{x}_0, \mathbf{p}; \boldsymbol{\beta}) = \mathbf{y}_0, \quad (15)$$

⁴Non-uniqueness here implies that there are infinitely many choices for functions \mathbf{l} , \mathbf{b} , \mathbf{g} , \mathbf{h} for which (11) holds true.

⁵When \mathbf{l} satisfies this condition we say that \mathbf{l} is a topological embedding of \mathbb{R}^{n_x} into \mathbb{R}^m [35].

such that:

$$\sup_{(t, \mathbf{x}_0, \mathbf{p}) \in E} (\|\psi(t, \mathbf{x}_0, \mathbf{p}) - \mathbf{d}(e(\mathbf{x}_0, \mathbf{p}; \boldsymbol{\beta}) + \boldsymbol{\tau}(t, \mathbf{x}_0, \mathbf{p}; \boldsymbol{\nu}) \circ \mathbf{c}(\mathbf{x}_0, \mathbf{p}; \boldsymbol{\alpha}); \boldsymbol{\theta})\|_2) \leq \varepsilon, \quad (16)$$

where each network \mathbf{d} , $\boldsymbol{\mathcal{E}}$, \mathbf{c} , and $\boldsymbol{\tau}$ belong to the appropriate class functions defined in definition 2 and satisfies:

$$\begin{aligned} \sup_{(t, \mathbf{x}_0, \mathbf{p}) \in E} \|\mathbf{l}^{-1}(\mathbf{g}(\mathbf{x}_0, \mathbf{p}) + \mathbf{h}(t, \mathbf{x}_0, \mathbf{p}) \circ \mathbf{b}(\mathbf{x}_0, \mathbf{p})) - \mathbf{d}(\mathbf{g}(\mathbf{x}_0, \mathbf{p}) + \mathbf{h}(t, \mathbf{x}_0, \mathbf{p}) \circ \mathbf{f}(\mathbf{x}_0, \mathbf{p}); \boldsymbol{\theta})\|_2 &\leq \frac{\varepsilon}{4}, \\ \sup_{(t, \mathbf{x}_0, \mathbf{p}) \in E} \|\mathbf{g}(\mathbf{x}_0, \mathbf{p}) - e(\mathbf{x}_0, \mathbf{p}; \boldsymbol{\beta})\|_2 &\leq \frac{\varepsilon}{4L}, \quad \sup_{(t, \mathbf{x}_0, \mathbf{p}) \in E} \|\mathbf{b}(\mathbf{x}_0, \mathbf{p}) - \mathbf{c}(\mathbf{x}_0, \mathbf{p}; \boldsymbol{\alpha})\|_2 \leq \frac{\varepsilon}{4Lc_2}, \\ \sup_{(t, \mathbf{x}_0, \mathbf{p}) \in E} \|\mathbf{h}(t, \mathbf{x}_0, \mathbf{p}) - \boldsymbol{\tau}(t, \mathbf{x}_0, \mathbf{p}; \boldsymbol{\nu})\|_2 &\leq \frac{\varepsilon}{4Lc_1}, \end{aligned}$$

where $\mathbf{l}(\mathbf{y})$, $\mathbf{g}(\mathbf{x}_0, \mathbf{p})$, $\mathbf{b}(\mathbf{x}_0, \mathbf{p})$, $\mathbf{h}(t, \mathbf{x}_0, \mathbf{p})$ are functions defined in lemma 2, L is the Lipschitz constant of $\mathbf{d}(\cdot; \boldsymbol{\theta})$ with respect to the first argument, $c_1 = \sup_{(\mathbf{x}_0, \mathbf{p}) \in E} \|\mathbf{b}(\mathbf{x}_0, \mathbf{p})\|_\infty$, $c_2 = \sup_{(t, \mathbf{x}_0, \mathbf{p}) \in E} \|\boldsymbol{\tau}(t, \mathbf{x}_0, \mathbf{p}; \boldsymbol{\nu})\|_\infty$.

Proof: Note that the analytical solution for the constant velocity latent dynamics (15) can be written as:

$$\mathbf{y}(\boldsymbol{\tau}) = e(\mathbf{x}_0, \mathbf{p}; \boldsymbol{\beta}) + \boldsymbol{\tau} \circ \mathbf{c}(\mathbf{x}_0, \mathbf{p}; \boldsymbol{\alpha}).$$

For any $(t, \mathbf{x}_0, \mathbf{p}) \in E$, define the error ρ between the ground truth flow map $\psi(t, \mathbf{x}_0, \mathbf{p})$ and the one predicted by LiLaN (for arbitrary choice of networks and it's parameters $\boldsymbol{\theta}$, $\boldsymbol{\beta}$, $\boldsymbol{\alpha}$, $\boldsymbol{\nu}$) as follows:

$$\rho = \|\psi(t, \mathbf{x}_0, \mathbf{p}) - \mathbf{d}(e(\mathbf{x}_0, \mathbf{p}; \boldsymbol{\beta}) + \boldsymbol{\tau} \circ \mathbf{c}(\mathbf{x}_0, \mathbf{p}; \boldsymbol{\alpha}); \boldsymbol{\theta})\|_2. \quad (17)$$

Now, using (14) in lemma 2, the error (17) can be rewritten as:

$$\rho = \|\mathbf{l}^{-1}(\mathbf{g}(\mathbf{x}_0, \mathbf{p}) + \mathbf{h}(t, \mathbf{x}_0, \mathbf{p}) \circ \mathbf{b}(\mathbf{x}_0, \mathbf{p})) - \mathbf{d}(e(\mathbf{x}_0, \mathbf{p}; \boldsymbol{\beta}) + \boldsymbol{\tau} \circ \mathbf{c}(\mathbf{x}_0, \mathbf{p}; \boldsymbol{\alpha}); \boldsymbol{\theta})\|_2$$

Adding and subtracting term $\mathbf{d}(\mathbf{g}(\mathbf{x}_0, \mathbf{p}) + \mathbf{h}(t, \mathbf{x}_0, \mathbf{p}) \circ \mathbf{b}(\mathbf{x}_0, \mathbf{p}); \boldsymbol{\theta})$ above and applying a triangle inequality we have:

$$\begin{aligned} \rho &= \|\mathbf{l}^{-1}(\mathbf{g}(\mathbf{x}_0, \mathbf{p}) + \mathbf{h}(t, \mathbf{x}_0, \mathbf{p}) \circ \mathbf{b}(\mathbf{x}_0, \mathbf{p})) - \mathbf{d}(e(\mathbf{x}_0, \mathbf{p}; \boldsymbol{\beta}) + \boldsymbol{\tau} \circ \mathbf{c}(\mathbf{x}_0, \mathbf{p}; \boldsymbol{\alpha}); \boldsymbol{\theta})\|_2 \\ &\leq \underbrace{\|\mathbf{l}^{-1}(\mathbf{g}(\mathbf{x}_0, \mathbf{p}) + \mathbf{h}(t, \mathbf{x}_0, \mathbf{p}) \circ \mathbf{b}(\mathbf{x}_0, \mathbf{p})) - \mathbf{d}(\mathbf{g}(\mathbf{x}_0, \mathbf{p}) + \mathbf{h}(t, \mathbf{x}_0, \mathbf{p}) \circ \mathbf{b}(\mathbf{x}_0, \mathbf{p}); \boldsymbol{\theta})\|_2}_I \\ &\quad + \underbrace{\|\mathbf{d}(\mathbf{g}(\mathbf{x}_0, \mathbf{p}) + \mathbf{h}(t, \mathbf{x}_0, \mathbf{p}) \circ \mathbf{b}(\mathbf{x}_0, \mathbf{p}); \boldsymbol{\theta}) - \mathbf{d}(e(\mathbf{x}_0, \mathbf{p}; \boldsymbol{\beta}) + \boldsymbol{\tau} \circ \mathbf{c}(\mathbf{x}_0, \mathbf{p}; \boldsymbol{\alpha}); \boldsymbol{\theta})\|_2}_{II} \end{aligned} \quad (18)$$

Now let us consider the term (I) in (18). Given the continuous functions \mathbf{l}^{-1} , \mathbf{g} , \mathbf{h} , \mathbf{b} , $\forall \varepsilon_1$ there exists a neural network $\mathbf{d}(\cdot; \boldsymbol{\theta}(\varepsilon_1)) \in \mathcal{N}_{m, n_x}^\phi$ with parameters $\boldsymbol{\theta}(\varepsilon_1)$ such that the following holds (the universal approximation result in [29, Theorem 3.2]):

$$\sup_{(t, \mathbf{x}_0, \mathbf{p}) \in E} \|\mathbf{l}^{-1}(\mathbf{g}(\mathbf{x}_0, \mathbf{p}) + \mathbf{h}(t, \mathbf{x}_0, \mathbf{p}) \circ \mathbf{b}(\mathbf{x}_0, \mathbf{p})) - \mathbf{d}(\mathbf{g}(\mathbf{x}_0, \mathbf{p}) + \mathbf{h}(t, \mathbf{x}_0, \mathbf{p}) \circ \mathbf{b}(\mathbf{x}_0, \mathbf{p}); \boldsymbol{\theta}(\varepsilon_1))\|_2 \leq \varepsilon_1, \quad (19)$$

Now let us consider the term (II) in (18). We have:

$$\begin{aligned} &\|\mathbf{d}(\mathbf{g}(\mathbf{x}_0, \mathbf{p}) + \mathbf{h}(t, \mathbf{x}_0, \mathbf{p}) \circ \mathbf{b}(\mathbf{x}_0, \mathbf{p}); \boldsymbol{\theta}) - \mathbf{d}(e(\mathbf{x}_0, \mathbf{p}; \boldsymbol{\beta}) + \boldsymbol{\tau} \circ \mathbf{c}(\mathbf{x}_0, \mathbf{p}; \boldsymbol{\alpha}); \boldsymbol{\theta})\|_2 \\ &\leq L \left(\underbrace{\|\mathbf{g}(\mathbf{x}_0, \mathbf{p}) + \mathbf{h}(t, \mathbf{x}_0, \mathbf{p}) \circ \mathbf{b}(\mathbf{x}_0, \mathbf{p}) - e(\mathbf{x}_0, \mathbf{p}; \boldsymbol{\beta}) + \boldsymbol{\tau} \circ \mathbf{c}(\mathbf{x}_0, \mathbf{p}; \boldsymbol{\alpha})\|_2}_{III} \right) \end{aligned} \quad (20)$$

where we have used the fact that $\mathbf{d}(\cdot; \boldsymbol{\theta}) \in \mathcal{N}_{m, n_x}^\phi$ is Lipschitz continuous (with constant L). Note that the Lipschitz continuity of \mathbf{d} is easily obtained by employing Lipschitz continuous activation functions. We can bound (III) in (20) triangle inequality as

$$\begin{aligned} & \|\mathbf{g}(\mathbf{x}_0, \mathbf{p}) + \mathbf{h}(t, \mathbf{x}_0, \mathbf{p}) \circ \mathbf{b}(\mathbf{x}_0, \mathbf{p}) - \mathbf{e}(\mathbf{x}_0, \mathbf{p}; \boldsymbol{\beta}) + \boldsymbol{\tau} \circ \mathbf{c}(\mathbf{x}_0, \mathbf{p}, \boldsymbol{\alpha})\|_2 \\ & \leq \underbrace{\|\mathbf{g}(\mathbf{x}_0, \mathbf{p}) - \mathbf{e}(\mathbf{x}_0, \mathbf{p}; \boldsymbol{\beta})\|_2}_{IV} + \underbrace{\|\mathbf{h}(t, \mathbf{x}_0, \mathbf{p}) \circ \mathbf{b}(\mathbf{x}_0, \mathbf{p}) - \boldsymbol{\tau} \circ \mathbf{c}(\mathbf{x}_0, \mathbf{p}, \boldsymbol{\alpha})\|_2}_{V}. \end{aligned} \quad (21)$$

For (IV) in (21), again by invoking [29, Theorem 3.2], we have $\forall \varepsilon_2$ there exists a neural network $e(\mathbf{x}_0, \mathbf{p}; \boldsymbol{\beta}(\varepsilon_2)) \in \mathcal{N}_{n_x+n_p, m}^\phi$ with parameters $\boldsymbol{\beta}(\varepsilon_2)$ such that,

$$\sup_{(t, \mathbf{x}_0, \mathbf{p}) \in E} \|\mathbf{g}(\mathbf{x}_0, \mathbf{p}) - e(\mathbf{x}_0, \mathbf{p}; \boldsymbol{\beta}(\varepsilon_2))\|_2 \leq \varepsilon_2. \quad (22)$$

Analyzing term (V) in (21), we have:

$$\begin{aligned} & \|\mathbf{h}(t, \mathbf{x}_0, \mathbf{p}) \circ \mathbf{b}(\mathbf{x}_0, \mathbf{p}) - \boldsymbol{\tau} \circ \mathbf{c}(\mathbf{x}_0, \mathbf{p}, \boldsymbol{\alpha})\|_2 \\ & = \|\mathbf{h}(t, \mathbf{x}_0, \mathbf{p}) \circ \mathbf{b}(\mathbf{x}_0, \mathbf{p}) - \boldsymbol{\tau} \circ \mathbf{b}(\mathbf{x}_0, \mathbf{p}) + \boldsymbol{\tau} \circ \mathbf{b}(\mathbf{x}_0, \mathbf{p}) - \boldsymbol{\tau} \circ \mathbf{c}(\mathbf{x}_0, \mathbf{p}, \boldsymbol{\alpha})\|_2 \\ & \leq \|(\mathbf{h}(t, \mathbf{x}_0, \mathbf{p}) - \boldsymbol{\tau}) \circ \mathbf{b}(\mathbf{x}_0, \mathbf{p})\|_2 + \|\boldsymbol{\tau} \circ (\mathbf{b}(\mathbf{x}_0, \mathbf{p}) - \mathbf{c}(\mathbf{x}_0, \mathbf{p}, \boldsymbol{\alpha}))\|_2 \\ & \leq \|\mathbf{F}_f(\mathbf{x}_0, \mathbf{p})(\mathbf{h}(t, \mathbf{x}_0, \mathbf{p}) - \boldsymbol{\tau})\|_2 + \|\mathbf{T}_\tau(t, \mathbf{x}_0, \mathbf{p})(\mathbf{b}(\mathbf{x}_0, \mathbf{p}) - \mathbf{c}(\mathbf{x}_0, \mathbf{p}, \boldsymbol{\alpha}))\|_2 \\ & \leq \|\mathbf{F}_f(\mathbf{x}_0, \mathbf{p})\|_2 \|\mathbf{h}(t, \mathbf{x}_0, \mathbf{p}) - \boldsymbol{\tau}\|_2 + \|\mathbf{T}_\tau(t, \mathbf{x}_0, \mathbf{p})\|_2 \|\mathbf{b}(\mathbf{x}_0, \mathbf{p}) - \mathbf{c}(\mathbf{x}_0, \mathbf{p}, \boldsymbol{\alpha})\|_2 \end{aligned} \quad (23)$$

where $\mathbf{F}_f(\mathbf{x}_0, \mathbf{p})$ is a diagonal matrix whose diagonal elements are $\mathbf{b}_i(\mathbf{x}_0, \mathbf{p})$ and $\mathbf{T}_\tau(t, \mathbf{x}_0, \mathbf{p})$ is a diagonal matrix whose diagonal elements are $\tau_i(t, \mathbf{x}_0, \mathbf{p}; \boldsymbol{\nu})$. From [29, Theorem 3.2], $\forall \varepsilon_3$ there exists a neural network $\mathbf{c}(\mathbf{x}_0, \mathbf{p}; \boldsymbol{\alpha}(\varepsilon_3)) \in \mathcal{N}_{n_x+n_p, m}^\phi$ such that,

$$\sup_{(t, \mathbf{x}_0, \mathbf{p}) \in E} \|\mathbf{b}(\mathbf{x}_0, \mathbf{p}) - \mathbf{c}(\mathbf{x}_0, \mathbf{p}; \boldsymbol{\alpha}(\varepsilon_3))\|_2 \leq \varepsilon_3, \quad (24)$$

and $\forall \varepsilon_4$ there exists a neural network $\boldsymbol{\tau}(t, \mathbf{x}_0, \mathbf{p}; \boldsymbol{\nu}(\varepsilon_4)) \in \mathcal{N}_{n_x+n_p+1, m}^\phi$ such that,

$$\sup_{(t, \mathbf{x}_0, \mathbf{p}) \in E} \|\mathbf{h}(t, \mathbf{x}_0, \mathbf{p}) - \boldsymbol{\tau}(t, \mathbf{x}_0, \mathbf{p}; \boldsymbol{\nu}(\varepsilon_4))\|_2 \leq \varepsilon_4. \quad (25)$$

Plugging the results (20), (21), (23) back in (18), the error ρ in (17) can now be bounded as follows:

$$\begin{aligned} \rho & = \|\boldsymbol{\psi}(t, \mathbf{x}_0, \mathbf{p}) - \mathbf{d}(\mathbf{e}(\mathbf{x}_0, \mathbf{p}; \boldsymbol{\beta}) + \boldsymbol{\tau} \circ \mathbf{c}(\mathbf{x}_0, \mathbf{p}, \boldsymbol{\alpha}); \boldsymbol{\theta})\|_2 \\ & \leq \|\mathbf{l}^{-1}(\mathbf{g}(\mathbf{x}_0, \mathbf{p}) + \mathbf{h}(t, \mathbf{x}_0, \mathbf{p}) \circ \mathbf{b}(\mathbf{x}_0, \mathbf{p})) - \mathbf{d}(\mathbf{g}(\mathbf{x}_0, \mathbf{p}) + \mathbf{h}(t, \mathbf{x}_0, \mathbf{p}) \circ \mathbf{b}(\mathbf{x}_0, \mathbf{p}); \boldsymbol{\theta})\|_2 \\ & + L (\|\mathbf{g}(\mathbf{x}_0, \mathbf{p}) - \mathbf{e}(\mathbf{x}_0, \mathbf{p}; \boldsymbol{\beta})\|_2 + \|\mathbf{F}_f(\mathbf{x}_0, \mathbf{p})\|_2 \|\mathbf{h}(t, \mathbf{x}_0, \mathbf{p}) - \boldsymbol{\tau}\|_2 + \|\mathbf{T}_\tau(t, \mathbf{x}_0, \mathbf{p})\|_2 \|\mathbf{b}(\mathbf{x}_0, \mathbf{p}) - \mathbf{c}(\mathbf{x}_0, \mathbf{p}, \boldsymbol{\alpha})\|_2) \\ & \leq \|\mathbf{l}^{-1}(\mathbf{g}(\mathbf{x}_0, \mathbf{p}) + \mathbf{h}(t, \mathbf{x}_0, \mathbf{p}) \circ \mathbf{b}(\mathbf{x}_0, \mathbf{p})) - \mathbf{d}(\mathbf{g}(\mathbf{x}_0, \mathbf{p}) + \mathbf{h}(t, \mathbf{x}_0, \mathbf{p}) \circ \mathbf{b}(\mathbf{x}_0, \mathbf{p}); \boldsymbol{\theta})\|_2 \\ & + L \sup_{(t, \mathbf{x}_0, \mathbf{p}) \in E} (\|\mathbf{g}(\mathbf{x}_0, \mathbf{p}) - \mathbf{e}(\mathbf{x}_0, \mathbf{p}; \boldsymbol{\beta})\|_2 + \|\mathbf{F}_f(\mathbf{x}_0, \mathbf{p})\|_2 \|\mathbf{h}(t, \mathbf{x}_0, \mathbf{p}) - \boldsymbol{\tau}\|_2) \\ & + L \sup_{(t, \mathbf{x}_0, \mathbf{p}) \in E} (\|\mathbf{T}_\tau(t, \mathbf{x}_0, \mathbf{p})\|_2 \|\mathbf{b}(\mathbf{x}_0, \mathbf{p}) - \mathbf{c}(\mathbf{x}_0, \mathbf{p}, \boldsymbol{\alpha})\|_2). \end{aligned} \quad (26)$$

Next, substituting (19), (22), (24) and (25) in (26), and by setting $\mathbf{d}(\cdot; \boldsymbol{\theta}) = \mathbf{d}(\cdot; \boldsymbol{\theta}(\varepsilon_1))$, $\boldsymbol{\tau} = \boldsymbol{\tau}(t, \mathbf{x}_0, \mathbf{p}; \boldsymbol{\nu}(\varepsilon_4))$, $\mathbf{c}(\mathbf{x}_0, \mathbf{p}; \boldsymbol{\alpha}) = \mathbf{c}(\mathbf{x}_0, \mathbf{p}; \boldsymbol{\alpha}(\varepsilon_3))$, $\mathbf{e}(\mathbf{x}_0, \mathbf{p}; \boldsymbol{\beta}) = \mathbf{e}(\mathbf{x}_0, \mathbf{p}; \boldsymbol{\beta}(\varepsilon_2))$, we have the following estimate for ρ :

$$\rho \leq \varepsilon_1 + L \left(\varepsilon_2 + \varepsilon_4 \times \sup_{(t, \mathbf{x}_0, \mathbf{p}) \in E} \|\mathbf{F}_f(\mathbf{x}_0, \mathbf{p})\|_2 + \varepsilon_3 \times \sup_{(t, \mathbf{x}_0, \mathbf{p}) \in E} \|\mathbf{T}_\tau(t, \mathbf{x}_0, \mathbf{p})\|_2 \right)$$

Now, by Weierstrauss extreme value theorem [36] we have $\sup_{(\mathbf{x}_0, \mathbf{p}) \in E} \|\mathbf{F}_f(\mathbf{x}_0, \mathbf{p})\|_2 \leq \sqrt{m} \sup_{(\mathbf{x}_0, \mathbf{p}) \in E} \|\mathbf{b}(\mathbf{x}_0, \mathbf{p})\|_\infty = c_1$ and $\sup_{(t, \mathbf{x}_0, \mathbf{p}) \in E} \|\mathbf{T}_\tau(t, \mathbf{x}_0, \mathbf{p})\|_2 \leq$

$\sqrt{m} \sup_{(t, \mathbf{x}_0, \mathbf{p}) \in E} \|\boldsymbol{\tau}(t, \mathbf{x}_0, \mathbf{p}; \boldsymbol{\nu}(\varepsilon_4))\|_\infty = c_2(\varepsilon_4)$. Also note that the Lipschitz constant L now depends on ε_1 due to the choice of parameter $\boldsymbol{\theta} = \boldsymbol{\theta}(\varepsilon_1)$ in (20) and we denote this dependence as $L(\varepsilon_1)$. Therefore, we have:

$$\rho \leq \varepsilon_1 + L(\varepsilon_1) \times (\varepsilon_2 + \varepsilon_4 \times c_1 + \varepsilon_3 \times c_2(\varepsilon_4)).$$

Finally, setting $\varepsilon_1 = \frac{\varepsilon}{4}$, $\varepsilon_2 = \frac{\varepsilon}{4L(\varepsilon_1)}$, $\varepsilon_4 = \frac{\varepsilon}{4L(\varepsilon_1)c_1}$, $\varepsilon_3 = \frac{\varepsilon}{4L(\varepsilon_1)c_2(\varepsilon_4)}$ concludes the proof.

Remark 3 (Independence of the latent dimension on the accuracy ε) *Theorem 1 shows that LiLaN can approximate the flow map, $\psi(t, \mathbf{x}_0, \mathbf{p})$, on a compact set to any degree of accuracy, ε , as long as the dimension of the latent dynamics is greater than or equal to the dimension the original dynamics (1). Further, the latent dimension does not depend on the accuracy ε .*

Remark 4 (Relaxing assumption in lemma 1) *Note that the assumption of $\mathbf{f}(\mathbf{x}(t), \mathbf{p})$ to be globally Lipschitz, is necessary to guarantee the existence of solution on the entire real line, for any $(\mathbf{x}_0, \mathbf{p}) \in \mathcal{G}_0 \times \mathcal{X}_p$. However, if it is known that the solution exists on some closed and bounded interval, $\tilde{I} = [0, \tilde{t}]$, for any $(\mathbf{x}_0, \mathbf{p}) \in \mathcal{G}_0 \times \mathcal{X}_p$, then the requirement for $\mathbf{f}(\mathbf{x}(t), \mathbf{p})$ to be globally Lipschitz can be relaxed. In such cases case, the set $E = I \times \mathcal{G}_0 \times \mathcal{X}_p$ in lemma 2 needs to be such that $I \subseteq \tilde{I}$. With these changes, the result in theorem 1 holds.*

For example, consider the Robertson Stiff Chemical Kinetics Model in section 3.1. In this case the solution $\mathbf{x}(t)$ of remains bounded in $[0, 1]$ for any time $t \in \mathbb{R}^+$ and $\forall \mathbf{p} \in \mathcal{X}_p$ (species concentration is always positive, and the sum of species concentration is 1 at any time). Based on the existence theorem in [37] (page 147), given that $\mathbf{f}(\mathbf{x}(t), \mathbf{p})$ is continuously differentiable with respect to both arguments and the solution does not leave the closed and bounded set $[0, 1]$, solution exists on \mathbb{R}^+ for any $\mathbf{p} \in \mathcal{X}_p$. Therefore, in this case we do not need $\mathbf{f}(\mathbf{x}(t), \mathbf{p})$ to be globally Lipschitz.

2.3 Architectural Variants

This section presents a few variants of LiLaN presented in section 2.1. There are several, simple modifications that can be made to create "stacked" variants of the architecture, similar to the DeepONet implementation in [24]. We tested the following four variants:

1. *The "Full learning" approach.* This approach is exactly the same as the one described in section 2.1. In particular, we have three encoders, $(\mathbf{e}, \mathbf{c}, \boldsymbol{\tau})$, and one decoder, \mathbf{d} . The description of each network is provided in section 2.1. A schematic of the approach is provided in figure 2.
2. *The "Independent learning" approach.* In this case, we have n_x triples of encoders, $(\mathbf{e}_i, \mathbf{c}_i, \boldsymbol{\tau}_i)$, where each triple encodes to a unique set of latent dynamics. Additionally, there are separate decoders, \mathbf{d}_i , for each i^{th} latent dynamics, which recovers the associated i^{th} component of the solution vector $\mathbf{x}(t)$ in (1), denoted as $\mathbf{x}_i(t)$. A schematic of the approach is provided in figure 3.
3. *The "Common encoder learning" approach.* In this case, we have three encoders, $(\mathbf{e}, \mathbf{c}, \boldsymbol{\tau})$, as described in section 2.1. However, we have n_x separate decoders, \mathbf{d}_i , which decode the same latent dynamics to recover the associated i^{th} component of the solution vector $\mathbf{x}(t)$ in (1). A schematic of the approach is provided in figure 4.
4. *The "Common decoder learning" approach.* In this case, we have n_x triples of encoders, $(\mathbf{e}_i, \mathbf{c}_i, \boldsymbol{\tau}_i)$, where each triple encodes to a unique set of latent dynamics. However, we have a single decoder, \mathbf{d} , which separately decodes each i^{th} latent dynamics to recover the associated i^{th} component of the solution vector $\mathbf{x}(t)$ in (1). A schematic of the approach is provided in figure 5.

Figure 6 shows the average point-wise relative error (42) (for a test data set), on the collisional-radiative charge state model in section 3.2, achieved by each approach presented above. Each approach was tested with approximately the same number of trainable parameters and the same training data. Based on the numerical result in figure 6, the

"independent learning" approach shows the best performance, for the given problem, illustrated by i) the error being the lowest on average for the full time series and ii) its error spike near $t = 10^{-8}s$, the region where the dynamics evolve quickly, being lowest. The "common decoder" approach struggled, never outperforming any other method for any period of time. The "common encoder" and "full" approaches, on the other hand, had competitive performance with one another. Though they were not more accurate than "independent learning," except near $t = 10^{-3}s$, where steady state is usually reached. However, the rapid increase of error at $t = 10^{-8}s$ for the "common encoder" approach was uniquely large, leading to a two order of magnitude increase in error. For all the ODE numerical results (sections section 3.1, section 3.2), we only present results for the "independent learning" approach, while for the PDE problems (sections section 3.3, section 3.4), we present results only for the "full" approach. Note that for PDE problems such as (32), a fine spatial discretization leads to a high-dimensional state space. As a result, the "independent learning" approach incurs a heavy computational cost during training, since using a separate network for each dimension results in a very large number of parameters (weights and biases). Hence, the results for the "independent learning" approach are not presented for PDE problems.

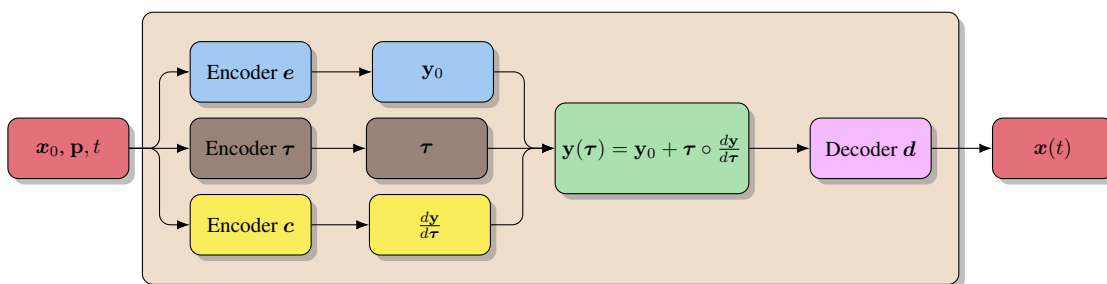


Figure 2: Schematic of the "full learning" approach.

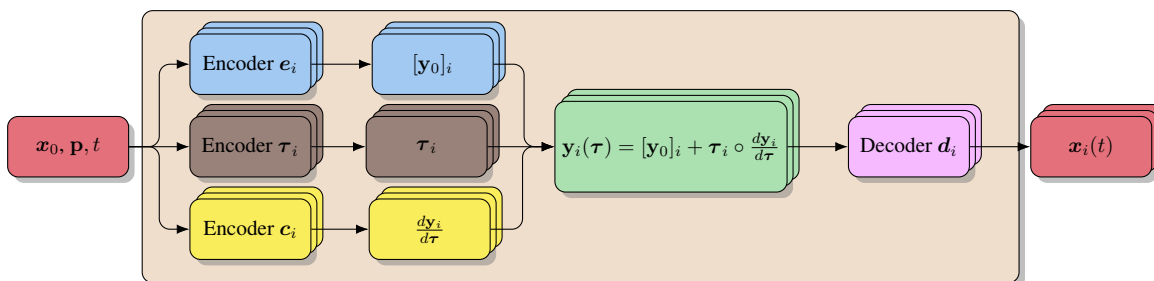


Figure 3: Schematic of "independent learning" approach.

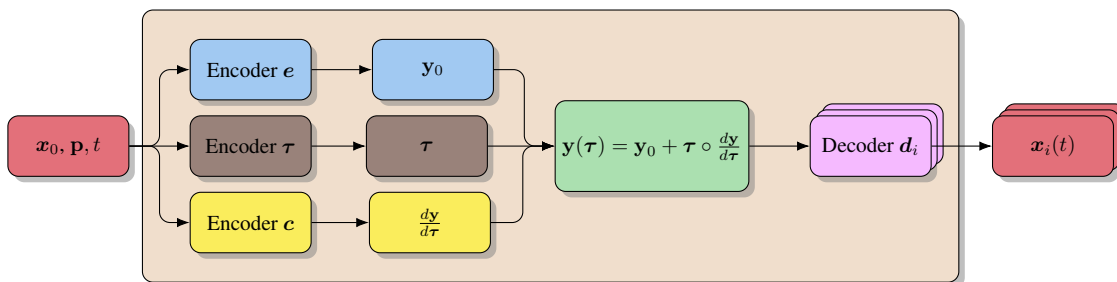


Figure 4: Schematic of "common encoder learning" approach: Note the single triple of encoder networks which map the initial conditions and parameters to the latent dynamics and n_x decoder networks which map from the latent space to the predicted solution.

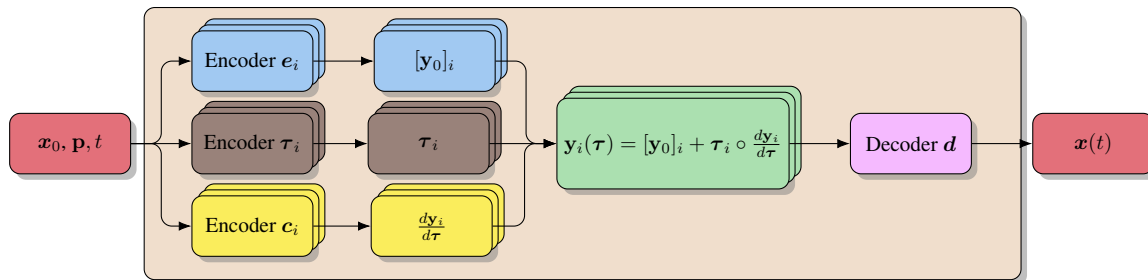


Figure 5: Schematic of "common decoder learning" approach: Note the n_x triples of encoder networks which map the initial conditions and parameters to the latent dynamics and single decoder network which maps from the latent space to the solution.

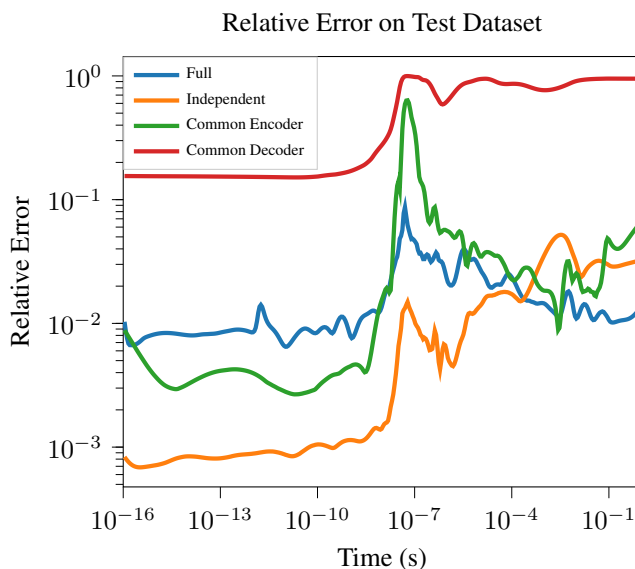


Figure 6: Average point-wise relative error (42), achieved by different approaches presented in section 2.3, for the full CR model (section 3.2) on the test dataset. The "independent" approach maintains the lowest error on average, and, in particular, has the least error near $t = 10^{-7} s$, in the fastest evolving temporal interval in the dynamics.

3 Numerical Experiments

In this section, we numerically demonstrate the effectiveness of LiLaN on a variety of prototype problems such as:

1. Robertson Stiff Chemical Kinetics Model [1]
2. Plasma Collisional-Radiative Model [2]
3. Allen-Cahn Phase Separation PDE [3]
4. Cahn-Hilliard Phase Separation PDE [3]

General experimental settings for all the problems and descriptions of methods adopted for comparison are detailed in Section A.

3.1 Robertson Stiff Chemical Kinetics Model

The Robertson chemical kinetics problem is a prototype stiff system of ODEs that describes the concentration of three species of reactants in a chemical reaction [1]. The model has been widely used to evaluate the performance of stiff

integrators in traditional numerical analysis. The reaction is characterized by the following system of ODEs:

$$\begin{aligned}\frac{dx_1}{dt} &= -p_1x_1 + p_3x_2x_3, \\ \frac{dx_2}{dt} &= p_1x_1 - p_3x_2x_3 - p_2x_2^2, \\ \frac{dx_3}{dt} &= p_2x_2^2,\end{aligned}\tag{27}$$

where the second species, x_2 , is the fastest evolving component and leads to numerical stiffness and difficulties in integration by explicit numerical solvers. In (27), the three reaction rates are typically chosen as $p_1 = 4 \cdot 10^{-2}$, $p_2 = 3 \cdot 10^7$, and $p_3 = 10^4$. Note that in (1), we have the parameters of the StODE as $\mathbf{p} = [p_1, p_2, p_3]$ and states as $\mathbf{x} = [x_1, x_2, x_3]$.

3.1.1 Data Generation

For a given initial condition, \mathbf{x}_0 , and parameters, \mathbf{p} , we integrate the system (27) with the Kvaerno5 stiff solver [38], from the `DiffraX` library [39], on a 50-point (i.e. $M = 50$ in (4)) logarithmically scaled time grid, spanning from $t = 10^{-5}s$ to $t = 10^5s$. In this problem, the initial condition is fixed as $\mathbf{x}_0 = [1, 0, 0]$ and the reaction rates \mathbf{p} vary across training samples. Similar to the data generation approach in [1], training input samples (p_1, p_2, p_3) were sampled from $[0.2 \cdot 10^{-2}, 0.6 \cdot 10^{-2}] \times [1.5 \cdot 10^7, 3.5 \cdot 10^7] \times [5 \cdot 10^3, 1.5 \cdot 10^4]$. The parameters of the training set, (p_1, p_2, p_3) , were sampled on a uniformly discretized grid of 16 linearly spaced collocation points in each domain. Thus, we consider a total of 4096 training samples. An additional 512 validation samples and 1000 test samples were generated using a uniformly discretized grid of 8 and 10 points in each domain respectively.

3.1.2 Results

LiLaN was tested and compared with the NODE [21], DeepONet [24], and the Sulzer and Buck I and II approaches. The choice of latent dimension m for each method is provided in table 8, Section A.6. Figure 7 shows a comparison of the average point-wise relative error, calculated via (42), for each method when applied to the test dataset. From figure 7, we see that LiLaN outperformed DeepONet by approximately one order of magnitude over the entire time, and also outperformed NODE by several orders of magnitude. Compared to Sulzer and Buck I and II, the performance of LiLaN is similar until the middle of the figure, where LiLaN takes the lead in accuracy. Note that the error of Sulzer and Buck I, the direct implementation of the methodology in [9], becomes greater than that of the modified Sulzer and Buck II with latent dimension expansion, which reveals the benefit of increasing the problem dimensionality. The computation is done using single-precision floats, which means the error is close to machine precision for prediction on the early steps of the time series. The average error achieved by different machine learning methods has been tabulated in table 1 and shows that LiLaN achieved the lowest error out of all the approaches, when evaluated on the test dataset. Table 1 also shows that the method by Sulzer and Buck [9] produced a competitive relative error compared to LiLaN. LiLaN outperformed NODE by two orders of magnitude and DeepONet by an order of magnitude. Figure 8 depicts a simulated trajectory using LiLaN for a randomly chosen set of parameters, \mathbf{p} , from the test dataset, where we observe the predicted solution matches closely to the one calculated by the numerical solver. In table 2, results on the speedup achieved over the chosen traditional numerical solver (Kvaerno5 stiff solver) have been tabulated, where it is presented that the LiLaN approach achieved over 800x speedup in the task of simulating trajectories from 1000 initial conditions.

3.2 Plasma Collisional-Radiative Model

In this section, we consider a collisional-radiative (CR) model, for a lithium plasma, which has more significant multiscale behavior in comparison to the Robertson problem, in addition to being stiff. The CR model is a nonlinear

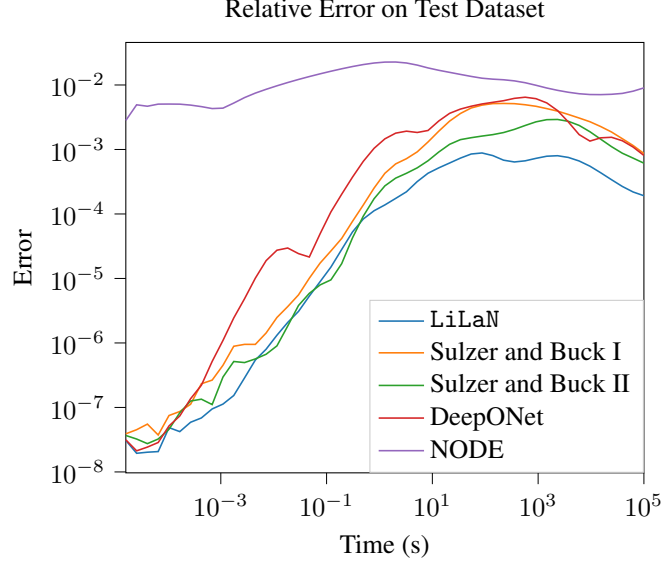


Figure 7: Average point-wise relative error over time (42) when evaluating Robertson chemical kinetics model on test data. All methods, besides NODE, performed well on this problem, with LiLaN having a slight performance edge due to greater accuracy at the end of the time series $t \in [10^0 s, 10^5 s]$.

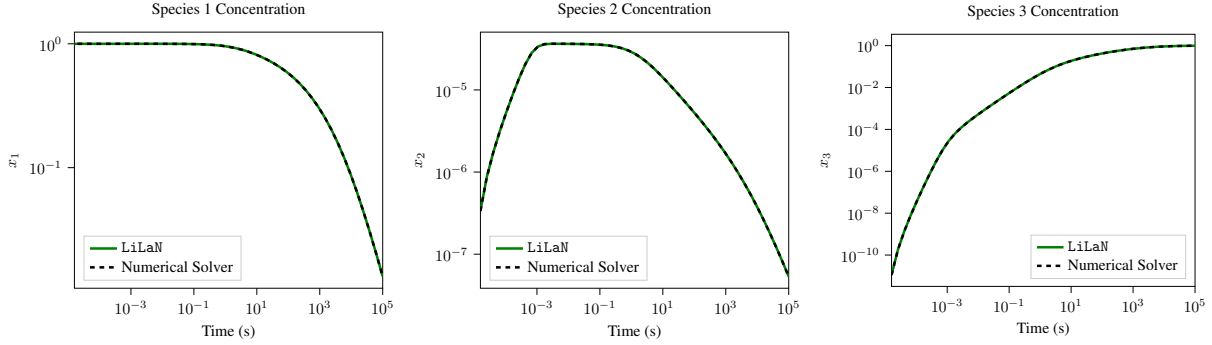


Figure 8: Simulated trajectory using LiLaN for a randomly chosen set of parameters \mathbf{p} , from the test dataset. Left to Right: Evolution of species x_1 with time; Evolution of species x_2 with time; Evolution of species x_3 with time. For each species, the LiLaN prediction is a near perfect visual match to the true dynamics.

dynamical system written as follows:

$$\frac{d\mathbf{n}}{dt} = \mathbf{R}(\mathbf{n}) \cdot \mathbf{n}, \quad \mathbf{n}(0) = \mathbf{n}_{initial}. \quad (28)$$

In eq. (28), $\mathbf{n} \in \mathbb{R}^{n_x}$ and \mathbf{R} is the $n_x \times n_x$ rate matrix with nonlinear dependence on \mathbf{n} . The rate matrix \mathbf{R} contains a set of rules for the up-transitions and down-transitions of electrons between the n_x discrete excited state levels of the state vector \mathbf{n} . The rate matrix explicitly depends on the temperature T_e and the electron density n_e . The dependence on temperature comes from the fact that the electron distribution is assumed to be a Maxwellian distribution, parameterized by T_e [40]. The electron density is defined as

$$n_e = \sum_{j=0}^Z j n_j, \quad (29)$$

where Z denotes the atomic number of the plasma element (in our simulation we consider lithium, for which $Z = 3$), j is the ion charge state, and n_j is the lithium ion density at charge state j given by (30) [40]. We have $L = 31$ in (30),

implying that $\mathbf{n} \in \mathbb{R}^{94}$, i.e. there are 94 discrete excited states, and

$$n_0 = \sum_{i=0}^{L-1} \mathbf{n}_i, \quad n_1 = \sum_{i=L}^{2L-1} \mathbf{n}_i, \quad n_2 = \sum_{i=2L}^{3L-1} \mathbf{n}_i, \quad n_3 = \mathbf{n}_{3L}. \quad (30)$$

The traditional approach to solving (28) are methods well suited for stiff problems, such as Backward Differentiation Formula (BDF) methods, described in detail in [41]. These approaches are implicit linear multistep methods and require solving a system of n_x equations at each time step. Solving this system becomes very expensive when n_x is large, as is the case for CR models with high-Z element impurities or when L is large.

3.2.1 Data Generation

For data generation, (28) is integrated using the six-step BDF formula on a 400-step (i.e. $M = 400$ in (4)) logarithmic time grid on $t \in [1^{-16}, 1^0]$. We generate different initial conditions $\mathbf{n}_{initial}$ for (28) through two parameters n_A and n_{per} as follows:

$$\begin{aligned} (\mathbf{n}_{initial})_0 &= (1 - n_{per} - 92 \cdot 10^{-5} \cdot n_{per}) \cdot n_A, \\ (\mathbf{n}_{initial})_1, (\mathbf{n}_{initial})_2, \dots, (\mathbf{n}_{initial})_{92} &= 10^{-5} \cdot n_{per} \cdot n_A, \\ (\mathbf{n}_{initial})_{93} &= n_{per} \cdot n_A, \end{aligned} \quad (31)$$

where $(\mathbf{n}_{initial})_i$ denotes the i^{th} component of $\mathbf{n}_{initial}$. We sample parameters (n_A, n_{per}, T_e) from $[10^{14}, 10^{15}] \times [1 \cdot 10^{-3}, 2 \cdot 10^{-3}] \times [5, 95]$, by considering a uniformly discretized grid (25 equally spaced collocation points) in each variable, to generate the training data. This leads to a total of 15625 training samples. Here, n_A is the total number of lithium ions, of all charge states, in the plasma, T_e is the temperature in KeV, and n_{per} is a constant used to parameterize the initial electron distribution. An additional 1000 validation samples and 4096 test samples were also generated using respective grids of 10 and 16 linearly discretized collocation points. Note that the sum of the entries in $\mathbf{n}_{initial}$ will be n_A . In fact, the total number of electrons is conserved for all time steps of the simulation. Note that in (1), we have the parameters $\mathbf{p} = [T_e, n_A]$ and $\mathbf{x}_0 = (\mathbf{n}_{initial}) = \mathcal{F}(\mathbf{n}_{\mathbf{p}})$, where $\mathbf{n}_{\mathbf{p}} = [n_A, n_{per}]$ and \mathcal{F} is a map determined by (31). In implementation, our approach only acts on the variables n_A, T_e, n_{per} , and t , and learning the parameterization (31) becomes part of the learning task.

3.2.2 Results

We demonstrate our approach on two cases:

1. CR charge state model: The aim here is to predict only the four charge states n_0, \dots, n_3 in (30).
2. Full CR model: The aim here is to predict the full state $\mathbf{n} \in \mathbb{R}^{94}$ in (28).

Results on the CR charge state model

LiLaN was tested and compared against NODE [21], DeepONet [24], the approach by Sulzer and Buck [9], as well as the modified Sulzer and Buck II. The choice of latent dimension m for each method is provided in table 8, Section A.6. The right subfigure of figure 9 shows a comparison of the average point-wise relative error, calculated via (42), for each method when applied to the test dataset. For this problem, we see that the error produced by LiLaN is lower than that of DeepONet. In particular, DeepONet has a large spike in error up to $\mathcal{O}(10^{-1})$ near $t = 10^{-8}s$, which is typically the beginning of the temporal region where rapid changes in the solution take place. The error increase is present in the error of LiLaN, but it is not as significant, with the error remaining on $\mathcal{O}(10^{-2})$. The error of DeepONet decreases to nearly the same value as that of LiLaN in the temporal region where the steady state is typically reached, $t \in [10^{-3}s, 10^0s]$. Additionally, NODE performs very poorly for this problem. Sulzer and Buck I and II produce a very close relative error to that of LiLaN throughout the simulation time, appearing marginally less accurate in the initial range $t \in [10^{-16}s, 10^{-10}s]$. The left subfigure of figure 9 depicts a simulated trajectory using LiLaN for a randomly chosen initial condition and set of parameters, \mathbf{x}_0, \mathbf{p} , from the test dataset. We observe that the predicted solution

closely matches the numerical solution. Table 1 shows that Sulzer and Buck II method produced slightly better relative error than LiLaN, when averaged over all time steps for all test samples. Sulzer and Buck I performed second best, followed very closely by LiLaN. The difference in their averaged test errors was approximately $1.1 \cdot 10^{-5}$. Table 1 also shows that DeepONet was an order of magnitude worse in terms of error than LiLaN and Sulzer and Buck I and II, while NODE was notably inaccurate, lagging three orders of magnitude behind. The speedup achieved over the chosen numerical solver (BDF6 method) of LiLaN was almost 1500x, when generating full trajectories from 1000 test initial conditions, as appears in table 2.

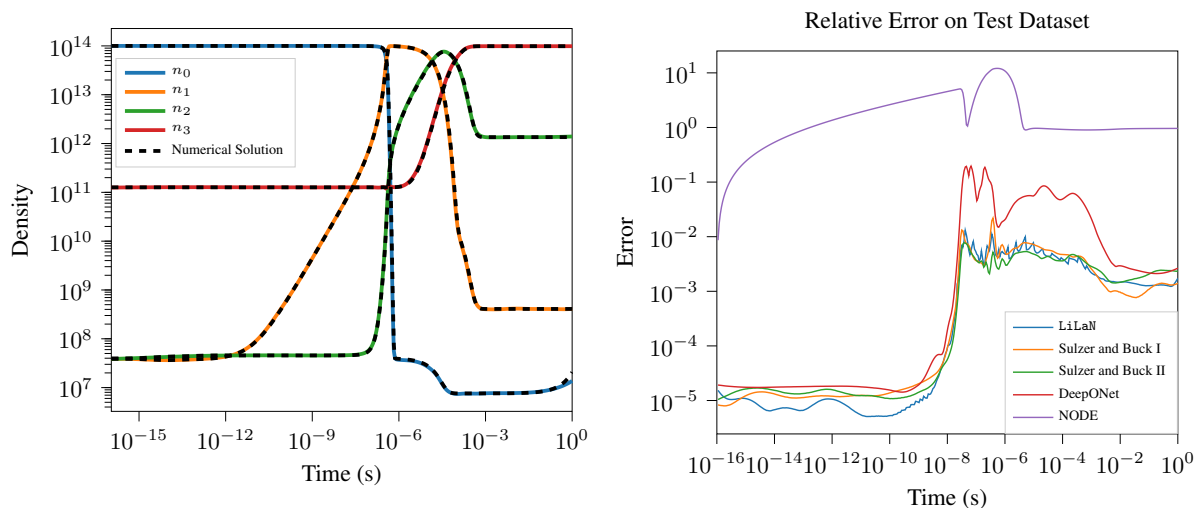


Figure 9: Left to Right: Comparison between numerical solution and machine learning prediction by LiLaN for a randomly chosen set of test initial conditions and parameters for CR charge state model (section 3.2). All four charge states are predicted with a high degree of accuracy; Average point-wise relative error over time (42) when evaluating CR charge state model on test data. LiLaN and Sulzer and Buck I and II have similar performance. DeepONet is slightly worse, with a larger error increase near $t = 10^{-8}s$. NODE struggles particularly.

Expanding Latent Space and Hidden Dimension

Figure 10 shows the change in training and test loss when different architectures are chosen, i.e. the dimension of the latent space and hidden layers were altered. For networks where the latent dimension was expanded (referred to as "latent dimension expansion" in figure 10), all hidden layers were held at 100 neurons, while the latent dimension was allowed to vary. The x-axis of figure 10, for the "latent dimension expansion" case, represents the ratio of the latent space dimension to the original problem dimension, i.e. $\frac{m}{n_x}$ in section 2.1. For networks where the hidden layer width was expanded (referred to as "hidden dimension expansion" in figure 10), the latent dimension multiplier was kept at one, indicating that the latent space has the same dimension as the original system. The x-axis of figure 10, for the "hidden dimension expansion" case, represents the number of neurons in each hidden layer. The result shows that much greater gains in accuracy are achieved by expanding the problem dimension to a higher-dimensional latent space. This agrees with our motivation during the development of LiLaN, namely, that lifting a stiff problem to higher-dimensional latent space makes the problem easier to solve with high accuracy. In contrast, expanding the dimension of hidden layers, while not allowing for latent expansion, resulted in very little gain in accuracy.

Results on the full CR model

To reduce the memory requirements associated with training the full CR model, we use 4096 data samples for training while 2500 samples are reserved for testing. The choice of latent dimension m for each method is provided in table 8, Section A.6. For this higher-dimensional problem, training a NODE was not computationally feasible on our hardware (NVIDIA Quadro RTX 5000) due to high memory requirements, even with the reduced training data set size. Hence, results for the NODE approach are not presented here. Figure 11 (right) shows a comparison of the average point-wise

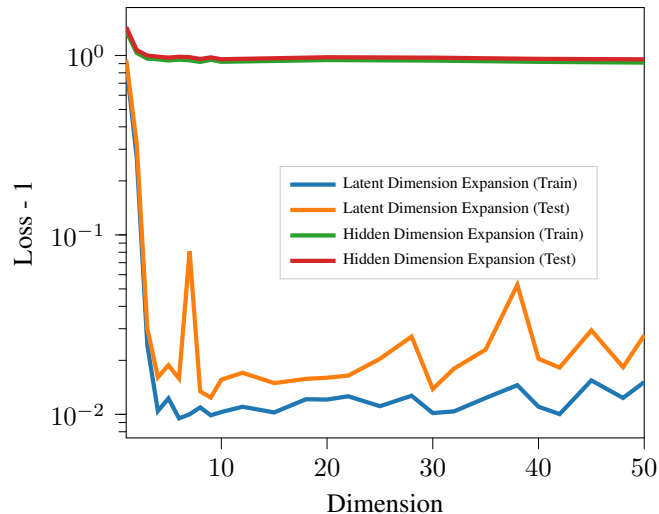


Figure 10: Training and testing loss achieved by different architectures. The x-axis, in the context of "latent dimension expansion", represents the ratio of the latent space dimension to the original problem dimension, i.e. $\frac{m}{n_x}$ in section 2.1. The x-axis, in the context of "hidden dimension expansion", represents the number of neurons in each hidden layer. Note that 1 is subtracted from the loss (40) because the minimum of the loss function is 1. A much greater decrease in loss is achieved when the latent dimension is increased in comparison to increasing the hidden layer width.

relative error, calculated via (42), for each method, when applied to the test dataset. We see that LiLaN outperformed all other methods. Another key observation from figure 11 (right) is that, while all of the methods have a spike in error near $t = 10^{-8}s$, LiLaN's error increase is the smallest by a wide margin, remaining on $\mathcal{O}(10^{-2})$, while Sulzer and Buck I reaches $\mathcal{O}(10^{-1})$ and DeepONet and Sulzer and Buck II increase to $\mathcal{O}(10^0)$. Recall from section 3.2.2, that $t = 10^{-8}s$ marks the approximate beginning of the region of the most rapid evolution of the dynamics, indicating that LiLaN handles this complex behavior, which is a significant challenge to predict, the best of all methods considered. Moving to the left subfigure of figure 11, there is a depiction of the solution to the CR model using LiLaN for a randomly chosen initial condition, \mathbf{x}_0 , and set of parameters, \mathbf{p} , from the test dataset. The figure shows that LiLaN produces a good approximation of the numerical solution. This approximation is particularly impressive near $t = 10^{-7}s$, where several components of the solution collapse in a nearly discontinuous manner. Again, the average error achieved by different machine learning methods has been tabulated in table 1, and additional results on the speedup achieved over the chosen traditional numerical solver (BDF6 method) have been tabulated in table 2. We observe from table 1 that LiLaN produced the lowest relative error in comparison to all other methods. LiLaN outperformed DeepONet and Sulzer and Buck I by one order of magnitude. Sulzer and Buck II did not perform well on this problem and had two orders of magnitude greater error than LiLaN. Table 2 reports the speedup achieved over the numerical solver (BDF6 method) by LiLaN, which was approximately 800x in the same experiment as described in sections 3.1 and 3.2.2 (CR charge state model).

3.3 Allen-Cahn PDE in 1D

The governing equation for the Allen-Cahn problem [3] is given below:

$$u_t = \varepsilon u_{xx} + u - u^3, \quad (32)$$

where the solution is $u(x, t)$. The equation describes phase separation in iron alloys and has a second order diffusive term and a cubic reaction term [3]. In order to write (32) in the form (1), the spatial domain is discretized and integrated as a system of ODEs by the method of lines [42]. The spatial domain, $x \in [0, 2\pi]$ is discretized by 201 linearly spaced

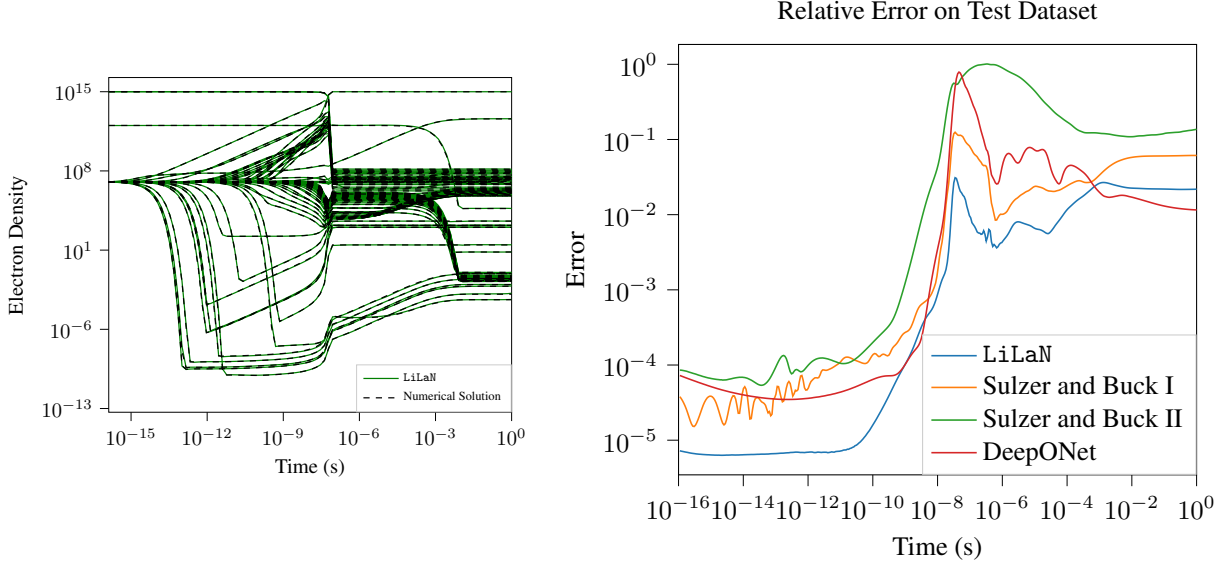


Figure 11: Left to Right: Comparison between numerical solution and machine learning prediction by LiLaN for a random set of test initial conditions and parameters for full CR model (section 3.2). The LiLaN’s prediction shows impressive accuracy for this highly-stiff, multiscale physics; Average point-wise relative error over time (42) when evaluating the full CR model on test data. Note that the LiLaN surrogate has the smallest error growth near $t = 10^{-8}s$, where the dynamics are evolving rapidly.

points leading to dimension $n_x = 201$ in (1). In the below discussions, \mathbf{x} denotes the vector containing the ordered set of discrete points on the spatial domain.

3.3.1 Data Generation

Initial conditions are generated using a sum of three sinusoidal waves as follows:

$$\mathbf{u}_0 = \sum_{i=1}^3 \alpha \sin(\beta \mathbf{x} + \phi) + \alpha \cos(\beta \mathbf{x} + \phi) \quad (33)$$

$$\alpha \sim \mathcal{U}(0, 1/6), \quad \beta \sim \mathcal{U}_{discrete}(1, 3), \quad \phi \sim \mathcal{U}(0, 2\pi), \quad (34)$$

where \mathcal{U} represents the continuous uniform distribution and $\mathcal{U}_{discrete}$ denotes the discrete uniform distribution. The amplitude α and phase ϕ are sampled from continuous uniform distributions, while the frequency β of each wave is sampled from a discrete uniform distribution where the frequencies 1, 2, or 3 are the discrete choices, each with equal probability of being selected. The integer frequencies ensure that the solution, \mathbf{u} , is periodic on the problem domain. After the construction of the initial conditions, each is evolved in time using the ETDRK4 explicit, exponential integrator proposed in [43]. The problem is solved over the time interval $t \in [0, 10]$ seconds, which is discretized by 101 linearly spaced points, (i.e. $M = 101$ in (4)). The dataset contains 900 samples for training, 100 samples for validation, and an additional 200 test samples, where each sample is a complete, time-integrated trajectory from a random initial condition generated by (33).

3.3.2 Results

The results for this problem are presented in figure 12, where the left subfigure shows the numerical solution, while the middle subfigure shows the solution produced by LiLaN, from the same random initial condition, unseen during training. We observe that the solutions are visibly identical. The right subfigure in figure 12 shows the absolute point-wise error between LiLaN and the numerical code. The errors are quite low nearly everywhere, except at phase boundaries

where the solution quickly switches between 1 and -1 , indicated by a quick shift from red to blue in the two leftmost subfigures of figure 12. This is a naturally challenging region to approximate, considering the sharp boundaries, yet the absolute pointwise error remains on $\mathcal{O}(10^{-2})$. In terms of performance over the entire test set, figure 13 presents the average error over time (42), for five machine learning approaches: LiLaN, Sulzer and Buck I and II, DeepONet, and NODE. Each approach is trained with the same data, hyperparameter settings, and approximately the same total number of trainable parameters. Additionally, the choice of latent dimension m for each method is provided in table 8, Section A.6. In figure 13, NODE performs slightly better than LiLaN during the initial, short time interval. This is because NODE begins integration from a known initial condition, \mathbf{x}_0 [21]. With no error accumulation at the starting point, the solution computed by NODE is most accurate in the vicinity of \mathbf{x}_0 . Figure 13 also shows that while LiLaN is particularly effective (with very low relative error) between 0s-7s, the approach by Sulzer and Buck [9] produced slightly lower error than LiLaN between 7s-10s. We also observe that the relative errors of all methods converge to similar values toward the end of the simulation, suggesting a need for further investigation. However, the reason could be that all of the methods are nearly equally good for predicting the steady state of the problem, a phenomenon that was observed between LiLaN, DeepONet, and Sulzer and Buck I and II in previous results sections 3.1 and 3.2.2 (figures 7 and 9). The average error achieved by different machine learning methods, for the Allen-Cahn PDE, are included in table 1, and report that the error produced by LiLaN is lowest in comparison to Sulzer and Buck I and II, DeepONet, and NODE, though they are all on the same order of magnitude. LiLaN achieved 14.3x speedup over the solver (ETDRK4 method), as shown in table 2. The experiment to test the speed of LiLaN versus the traditional solver is the same as in section 3.1. The speedup is less radical than previous results sections because exponential integrators are already extremely efficient for simulating stiff PDEs, meaning any speedup is a significant success.

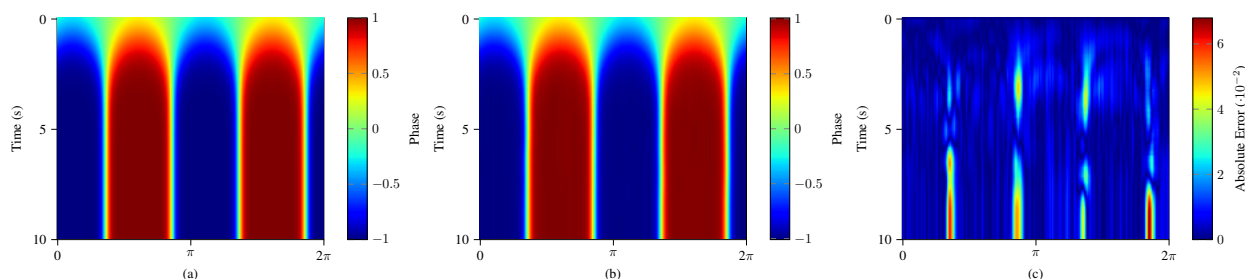


Figure 12: Left to right: Prediction by numerical method for Allen-Cahn PDE (section 3.3); Prediction by LiLaN; Point-wise absolute error between the two approaches. The largest errors are concentrated on sharp phase boundaries.

3.4 Cahn-Hilliard PDE in 1D

The governing equation for the Cahn-Hilliard problem [3] is given below:

$$u_t = \alpha (-u_{xx} - \gamma u_{xxxx} + (u^3)_{xx}) \quad (35)$$

where the solution is $u(x, t)$. This is another equation describing phase separation in alloys, but with much more complex physics due to the presence of the higher-order derivatives in the governing equation. Just as with the Allen-Cahn problem (section 3.3), the spatial domain is discretized and integrated as a system of ODEs by the method of lines [42]. The spatial domain, $x \in [-1, 1]$ is discretized by 201 linearly spaced points, and is denoted by \mathbf{x} in the below discussions.

3.4.1 Data Generation

Initial conditions in the Cahn-Hilliard problem are generated as follows:

$$\mathbf{u}_0 = \alpha \sin(\beta\pi(\mathbf{x} + 1) + \phi) + \alpha \cos(\beta\pi(\mathbf{x} + 1) + \phi), \quad (36)$$

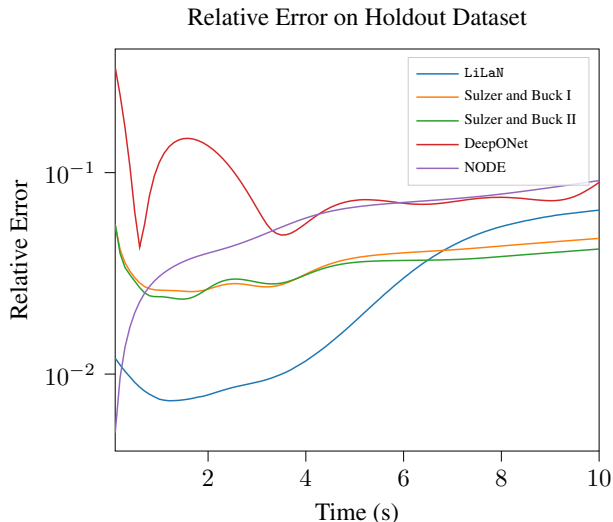


Figure 13: Average point-wise relative error over time (42) when evaluating Allen-Cahn PDE (section 3.3) on test data, for five machine learning approaches. Note that LiLaN has the best accuracy in first six seconds where the phase separation dynamics take place, while all methods converge to similar errors in the later time region where steady state is typically reached and there is no more evolution in the solution.

$$\alpha \sim \mathcal{U}(0.1, 0.6), \quad \beta \sim \mathcal{U}_{discrete}(1, 3), \quad \phi \sim \mathcal{U}(0, 2\pi), \quad (37)$$

where \mathcal{U} represents the continuous uniform distribution and $\mathcal{U}_{discrete}$ denotes the discrete uniform distribution. For each initial condition, generated by (36), the amplitude α and phase ϕ are sampled from continuous uniform distributions, specified in (37), while the frequency coefficient β of the wave is sampled from a discrete uniform distribution where the frequencies 1, 2, or 3 are the discrete choices, each with equal probability of being selected. The integer frequencies ensure that the solution, \mathbf{u} , is periodic on the problem domain. After the construction of the initial conditions, each is evolved in time using the ETDRK4 explicit, exponential integrator [43]. The problem is solved over the time interval $t \in [0, 20]$ seconds, which is discretized by 401 linearly spaced points (i.e. $M = 401$ in (4)). The dataset contains 900 samples for training, 100 samples for validation, and an additional 200 test samples, where each sample is a complete, time-integrated trajectory from a random initial condition generated by (36).

3.4.2 Results

Figure 14 (left) shows a solution generated by numerical code, while figure 14 (middle) shows the solution produced by LiLaN, from the same initial condition that was not seen during training. The solutions are strikingly similar visibly. Figure 14 (right) shows the absolute point-wise error between our approach and the numerical code for the example initial condition considered. Notice that on this problem, the largest errors are not at steady state phase boundaries, in contrast to the Allen-Cahn PDE results from section 3.3. Instead, high errors are most prevalent in the initial transient evolution before the solution reaches steady state, while the steady state has lower error than in section 3.3. In terms of performance over the entire test set, figure 15 depicts the average error over time (42), for LiLaN, Sulzer and Buck I and II, DeepONet, and NODE. Each approach is trained with the same data, hyperparameter settings, and approximately the same total number of trainable parameters. Again, the choice of latent dimension m for each method is provided in table 8, Section A.6. From figure 15 we see that LiLaN outperformed both NODE and DeepONet for prediction on the Cahn-Hilliard PDE. NODE performs slightly better than LiLaN during the initial, short time interval. The reason for this has been highlighted in section 3.3.2. We also observe that the approach of Sulzer and Buck I and II produce a very close relative error to that of LiLaN towards the end of the simulation time. This, again, could be due to the fact that predicting the steady state is easier than predicting the time dependent evolution. Looking at the example in figure 14, the evolution is done before $t = 3s$, which is typical across the entire dataset, with some exceptions where the evolution

is slower. Now, the region of figure 15 prior to $t = 4s$ is where LiLaN performs the best, beating all other methods, suggesting that it is uniquely suited for handling the time dependent portion of the solution. Table 1 illustrates that the average relative error produced by LiLaN is lowest of all methods tested. Significantly, DeepONet has an order of magnitude greater error than LiLaN, while the Sulzer and Buck I and II and NODE methods, though less accurate than LiLaN, achieve errors on the same order of magnitude. The speedup achieved over the chosen traditional numerical solver (ETDRK4 method) is tabulated in table 2, showing that LiLaN was 13.7x faster when generating full trajectories from 1000 test initial conditions. Again, even though the speedup is less than that of the ODE problems, it is still impressive due to the competition being conducted against an exponential integrator.

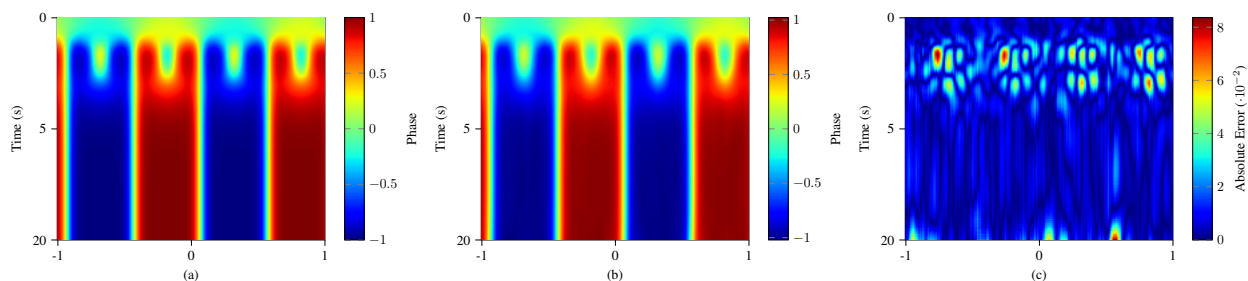


Figure 14: Left to right: Prediction by numerical method for Cahn-Hilliard PDE (section 3.4); Prediction by LiLaN; Point-wise absolute error between the two approaches. The error concentrates early in the evolution, near phase boundaries, while steady state phase boundaries do not have as much significant error seen in section 3.3.

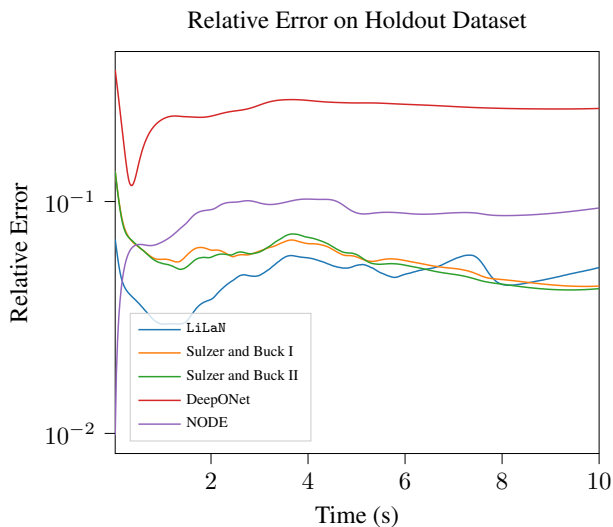


Figure 15: Average point-wise relative error over time (42) when evaluating Cahn-Hilliard PDE (section 3.4) on test data, for five machine learning approaches.

3.5 Improving Training Efficiency of LiLaN

Thus far, all previous sections have presented results for LiLaN training in the data-rich regime. In each problem considered, data is relatively cheap, but this may not hold true for other engineering tasks which require surrogate modeling. Therefore, it provides valuable insight to investigate the accuracy of the LiLaN model in the data-poor regime. On the other hand, a data-intensive training procedure can pose a heavy computational burden for training any model. This is especially the case when using large networks for high-dimensional problems (for example, the PDE problems in sections 3.3 and 3.4). In situations where the available memory or training time budget have strict limitations, data reduction is an effective tool to meet project requirements. This being the case, the accuracy of LiLaN surrogates under

different data reduction schemes must be examined. In this section, we consider two data reduction procedures and their ramifications for LiLaN:

1. The first strategy involves reducing the training data and investigating the effect on the generalization performance of LiLaN. In particular, we study how reducing the number of sample trajectories (i.e. the parameter N in (4)) affects the performance of LiLaN. Note that smaller training datasets significantly improve the computational efficiency during training while also reducing the data generation time. Additionally, in some applications, data cannot be generated at will and is limited to data from real-world sensor observations. For these reasons, it is highly desirable that the LiLaN architecture is robust and can achieve a high degree of generalization accuracy with varying amounts of data.
2. The second strategy involves the use of coarsened time discretizations in training, meaning reduction of the parameter M in (4) and investigating the impact on the generalization performance of LiLaN. Reducing the discretization of training data means potentially massive savings on memory during training. This, in turn, means that one can use a greater number of samples for a fixed training memory budget or can simply reap the rewards of lower memory cost and faster training speed.

3.5.1 Reducing Training Sample Size N in (4)

The first strategy for improving the training efficiency of LiLaN considers reducing the number of sample trajectories (i.e. the parameter N in (4)). For the Robertson (section 3.1) and full CR models (section 3.2.2), the original network was trained with 4096 samples from a three-dimensional parameter space. To understand how the prediction accuracy degrades with training data size, several smaller datasets were created by repeatedly reducing the number of training samples by a factor of two. For the CR charge state model (section 3.2.2), the initial training utilized 15625 samples from a three-dimensional parameter input space. For this problem, smaller datasets were created by repeatedly reducing the number of training samples, this time by a factor of five. The smallest dataset, for each ODE problem considered, contained only the eight corners of the original 3-dimensional parameter space.

From figure 16 (left subfigure) we see that for the Robertson model (section 3.1), using only 128 samples, a LiLaN can be trained to achieve error on the same order of magnitude as a network of the same architecture trained with 4096 samples (a reduction of 32x). For the CR charge state model (figure 16, (middle subfigure)), 125 samples were required to train a network which achieved error on the same order of magnitude of the original network trained with 15625 samples. Finally, after 256 training samples, the LiLaN's final accuracy on the full CR test dataset does not significantly improve if more samples are provided, as seen in figure 16 (right subfigure). From these ODE problem results, we observe that the amount of data used for training LiLaN surrogates can be reduced significantly while maintaining accuracy, indicating that data reduction via reducing the training samples is a viable data reduction strategy.

For completeness, the same sample reduction experiment was performed on each of the two PDE problems (sections 3.3 and 3.4). In each case, the original dataset of 900 samples was repeatedly reduced by 100 samples and used to train a new model. The smallest dataset contained 100 total sample trajectories. The change in accuracy with respect to sample size is shown in figure 17. Figure 17 shows that for each of the PDE problems, adding more samples typically resulted in a significant decrease in the relative error, though this decrease does slow after the first few hundred samples are added in both cases. However, this does suggest that reducing the training data may not be a favorable option for improving the computational efficiency, as these problems might require a large number of samples to guarantee a low relative error.

3.5.2 Using Coarse Time Discretizations in Training

An additional strategy to reduce the data and memory requirements of training the network is to consider a coarse time grid for the sample trajectories. In this section, we investigate the effect of reducing the parameter M in (4) on the performance of LiLaN. We consider different time discretizations by removing large numbers of time steps from

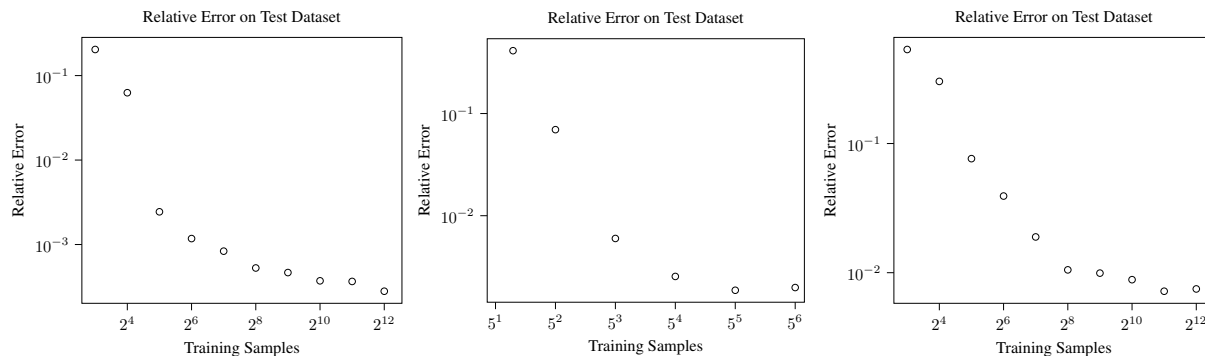


Figure 16: Left to Right: Average point-wise relative error over time (43) when evaluating Robertson chemical kinetics model (section 3.1) on test data (each plotted point shows the accuracy in relation to the number of training samples); Average point-wise relative error over time (43) when evaluating CR charge state model (section 3.2) on test data; Average point-wise relative error over time (43) when evaluating full CR model (section 3.2) on test data.

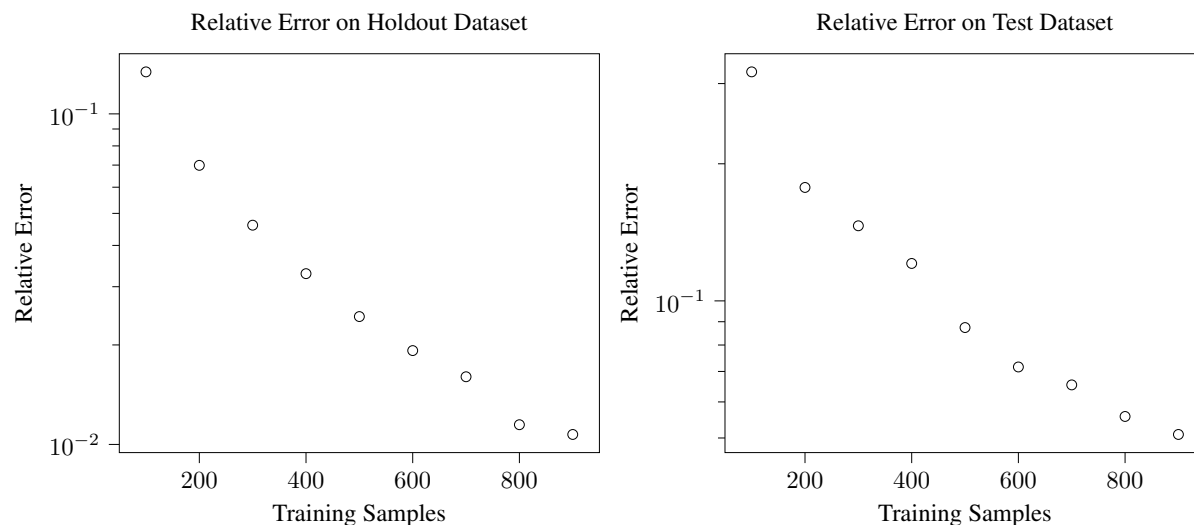


Figure 17: Left to Right: Average point-wise relative error over time (43) when evaluating Allen-Cahn PDE (section 3.3) on test data (each plotted point shows the accuracy in relation to the number of training samples); Average point-wise relative error over time (43) when evaluating Cahn-Hilliard PDE (section 3.4) on test data (each plotted point shows the accuracy in relation to the number of training samples) (43) on test data.

the training and validation data and using this new dataset to train the networks. Examples of different time grids considered for training neural networks are shown in figures 18, 19, 20, 21 and 22 (left subfigures). For assessing the performance, we retain the original test data, which still has a fine discretization in time. The main purpose of this study is to investigate whether coarsening the discretization in time is an effective means to reduce data, while maintaining the test accuracy of LiLaN.

Our results indicate that, in all test problems, data reduction by coarsening the underlying time discretization of data trajectories proves to be an effective path to reducing computational cost while maintaining test accuracy. The results of our experiments are shown in figures 18, 19, 20, 21 and 22. The left subfigure in each of the aforementioned figures depicts the new time discretizations used in training, while the right subfigure shows the change in relative error compared to how many steps were skipped. The x-axis of the right subfigures, labeled "Skipped Steps," indicates the number of time steps which were removed between steps in the original discretization. For example, if skipped steps = 10, then we retain the time steps $\{x_i\}_{i=0, 10, 20, \dots, M-10, M}$ for each training and validation sample. It is important to note that the accuracy reported is still evaluated on the test dataset, which is not downsampled in time. In each of

figures 18, 19, 20, 21 and 22, the results indicate that a significant number of time steps can be removed from the training discretization before accuracy degrades significantly. Specifically, figure 18, shows that on the Robertson ODE problem (section 3.1), we may take skipped steps = 8 before seeing the first major drop in accuracy. For the CR charge states and full CR models (section 3.2), figures 19 and 20 show that generalization error does not decrease until 20 steps are skipped between each preserved step. In the case of the Allen-Cahn PDE (section 3.3), figure 21 suggests that accuracy deteriorates very slowly in relation to the number of skipped steps, again with a falling off observed after gaps of 20 are removed from the data. For the final problem considered, in figure 22 we see that skipping a remarkable 40 steps results in almost no loss of test performance, and finally after 80 steps there is a larger decline in accuracy for the Cahn-Hilliard PDE (section 3.4). These results lead us to believe that coarsening the time discretization of the data is a very effective data reduction technique for LiLaN surrogates. However, the ability to train on coarse discretizations naturally begs the question of why LiLaN is so effective after data is reduced in this manner. To attempt to answer this question we devised an additional experiment to determine whether the time transformation network, τ , plays a significant role in LiLaN robustness to training on temporally downsampled discretizations of the original training data.

3.6 Importance of Learned Time Transformation

In this section, we investigate the importance of the nonlinear time transformation ($\tau(t, \mathbf{x}_0, \mathbf{p}; \nu)$ in (3)) on all problems considered in this work. The following experiments were inspired by the results on temporally downsampling training data, presented in figure 16. Additionally, since one of the key differences between LiLaN and the methodology of Sulzer and Buck [9] is the learned, nonlinear transformation of the time variable, we thought it informative to test the results of the LiLaN architecture if the time transformation was removed. In particular, instead of (3), we consider the solution in the latent space to have the following form:

$$\mathbf{y}(t, \mathbf{x}_0, \mathbf{p}) = \mathbf{e}(\mathbf{x}_0, \mathbf{p}; \beta) + t \mathbf{c}(\mathbf{x}_0, \mathbf{p}; \alpha). \quad (38)$$

where time, t , is first log scaled with the base 10 logarithm and then rescaled to the range $[0, 1]$. This new transform of the time variable is the same as used in [9]. The right subfigure of figures 18, 19, 20, 21 and 22 explore the benefit of the time transformation in the context of data reduction described in section 3.5.2. The black circles represent the error for LiLaNs trained with a learned time transformation, while the red dots indicate the error for LiLaNs trained with the simple, rescaled time variable. For the rest of this section, we will refer to the LiLaNs trained without using a time transformation τ network as LiLaN $_{\not\tau}$. Observing the right subfigures of figures 19, 21 and 22, we see a clear benefit in terms of final relative error achieved when using LiLaN over LiLaN $_{\not\tau}$. Specifically, there are two important features to recognize in each figure. First, in each case, the error is lower for LiLaN. Second, when coarsening the time discretization of training data, the accuracy of LiLaN $_{\not\tau}$ degrades significantly more quickly. On the CR charge state model (figure 19 right subfigure), LiLaN with skipped steps = 20 outperformed LiLaN $_{\not\tau}$ with skipped steps = 12. For the Allen-Cahn PDE (figure 21 right subfigure) LiLaN with skipped steps = 20 achieved lower error than a LiLaN $_{\not\tau}$ with skipped steps = 10. For the Cahn-Hilliard PDE (figure 22 right subfigure) LiLaN with skipped steps = 50 outperformed a LiLaN $_{\not\tau}$ with skipped steps = 25. These results suggest that the learned time transformation helps the LiLaN architecture in modeling the time dependence of the underlying dynamical system with fewer temporal data points. This result also reinforces the claims from sections 3.2.2, 3.3 and 3.4 that LiLaN is very good at modeling time dependent behaviors. In situations where memory budget is very limited or a large number of initial conditions must be trained over, LiLaN will be the better choice of architecture, in comparison to LiLaN $_{\not\tau}$, since each sample trajectory will require fewer snapshots in time, which greatly reduces the memory impact in training for each sample trajectory.

For the Robertson ODE and full CR model, shown in the right subfigures of figures 18 and 20 respectively, we did not observe significant benefits of a learned time transformation. Therefore, we conclude that the importance of the learned time transformation is problem dependent, however in the majority of cases investigated in our work, LiLaN allowed for greater data reduction than LiLaN $_{\not\tau}$. Considering the fact that the additional training cost associated with training

the time transformation network τ is negligible, the use of LiLaN (with time transformation τ) is generally advisable, instead of LiLaN γ .

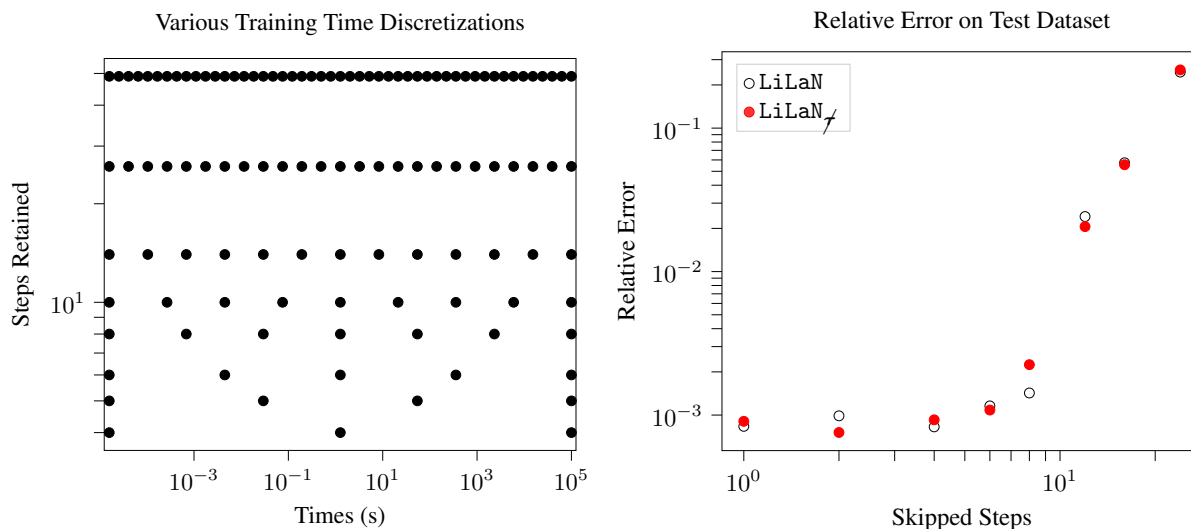


Figure 18: Effect of downsampling data in time (for training) on the prediction accuracy for the Robertson ODE (section 3.1). Left to Right: Examples of different time grids considered for training neural networks; Average point-wise relative error over time (43) on the test data. The relationship shown indicates that significant downsampling in time can be performed without losing accuracy. For this problem, LiLaN and LiLaN γ have a similar performance decay under temporal data coarsening.

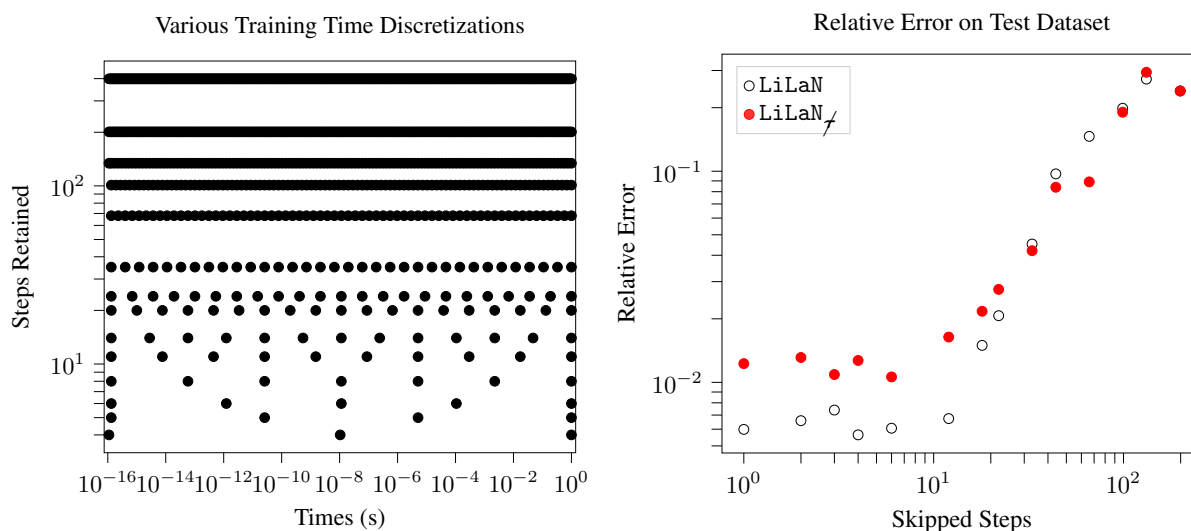


Figure 19: Effect of downsampling data in time (for training) on the prediction accuracy for CR charge state model (section 3.2). Left to Right: Examples of different time grids considered for training neural networks; Average point-wise relative error over time (43) on test data. The relationship shown indicates that significant downsampling in time can be performed without losing accuracy. For this problem, LiLaN has a slower accuracy decay than LiLaN γ under temporal data coarsening.

4 Summary of results

Table 1 shows the prediction error computed using (43) for each machine learning method, on each problem. We see that LiLaN produced the lowest relative error for all the problems except the CR charge state problem, where the Sulzer

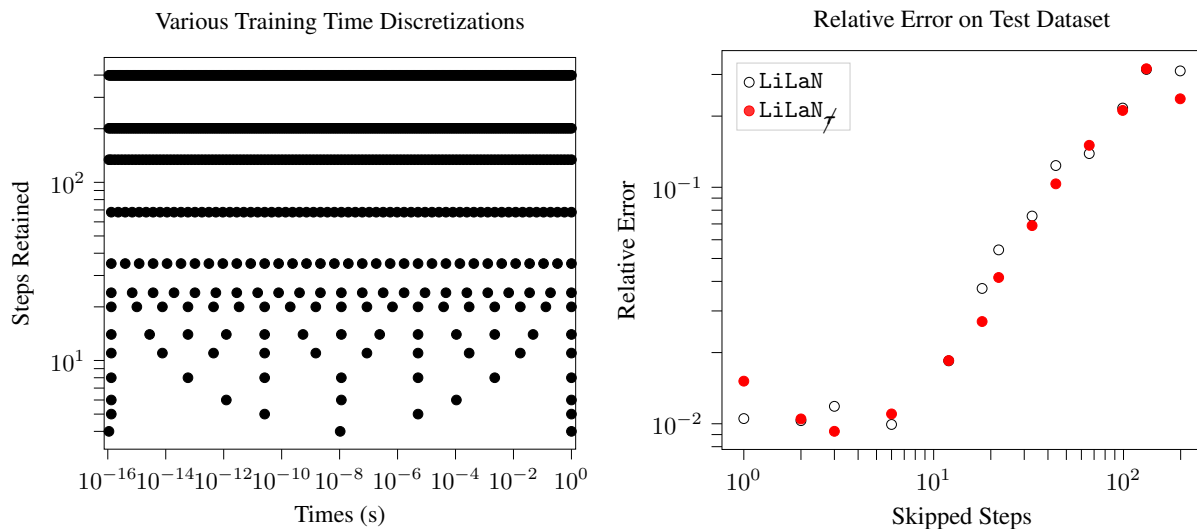


Figure 20: Effect of downsampling data in time (for training) on the prediction accuracy for the full CR model (section 3.2). Left to Right: Examples of different time grids considered for training neural networks; Average point-wise relative error over time (43) when evaluating full CR model on test data. The relationship shown indicates that significant downsampling in time can be performed without losing accuracy. For this problem, LiLaN and LiLaN_≠ have a similar performance decay under temporal data coarsening.

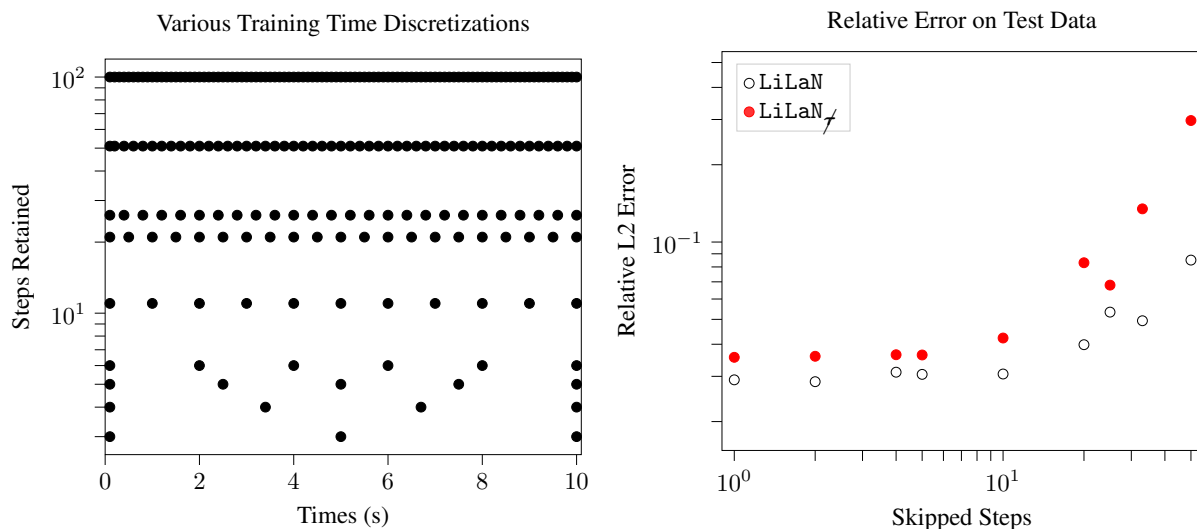


Figure 21: Effect of downsampling data in time (for training) on the prediction accuracy for the Allen-Cahn PDE (section 3.3). Left to Right: Examples of different time grids considered for training neural networks; Average point-wise relative error over time (43) on test data. The relationship shown indicates that significant downsampling in time can be performed without losing accuracy. For this problem, LiLaN has a slower accuracy decay than LiLaN_≠ under temporal data coarsening.

and Buck II approach, a modified form of the method in [9], slightly outperformed LiLaN, though the errors were on the same order of magnitude. Table 1 also shows that for the Robertson ODE Model section 3.1, LiLaN outperformed NODE by approximately two order of magnitude and outperformed DeepONet and Sulzer and Buck I by one order of magnitude in terms of the relative error achieved. For the CR charge state model, LiLaN and Sulzer and Buck I and II achieved errors on the same order of magnitude which were three and one orders of magnitude less than the errors of NODE and DeepONet respectively. For the full CR model, DeepONet and Sulzer and Buck I exceeded the error of LiLaN by an order of magnitude. On the same problem, Sulzer and Buck II struggled significantly compared to LiLaN,

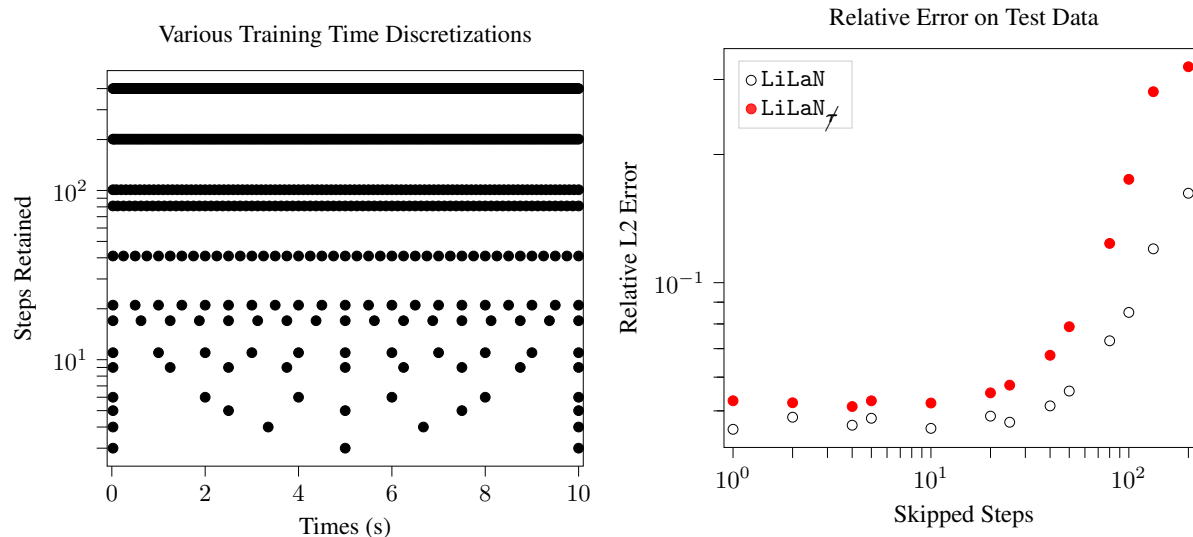


Figure 22: Effect of downsampling data in time (for training) on the prediction accuracy for the Cahn-Hilliard PDE (section 3.4). Left to Right: Examples of different time grids considered for training neural networks; Average point-wise relative error over time (43) on test data. The relationship shown indicates that significant downsampling in time can be performed without losing accuracy. For this problem, LiLaN has a slower accuracy decay than LiLaN \setminus under temporal data coarsening.

having two orders of magnitude greater relative error. On the two PDE problems, all methods had the same order of magnitude error, on the test dataset; however, LiLaN's was quantitatively the lowest. The one notable exception was DeepONet, which had one order of magnitude greater error on the Cahn-Hilliard problem compared to the other methods.

Table 2 shows the speedup of LiLaN in comparison to the traditional stiff numerical solver used to generate the data in each problem. To measure the speedup achieved, 1000 initial conditions were chosen to run the simulations for each problem. Table 2 shows the total time taken by both the numerical solver and LiLaN to compute the solutions for all the 1000 initial conditions. We see that LiLaN achieved $\mathcal{O}(10^1)$ - $\mathcal{O}(10^3)$ speedup on all problems, in terms of wall clock computation time, with especially remarkable speedup displayed on the three ODE problems (sections 3.1 and 3.2).

Table 1: Relative error on test data for the three machine learning approaches

Relative Error					
Problem	Robertson	CR charge state	Full CR model	Allen-Cahn	Cahn-Hilliard
NODE	$1.112 \cdot 10^{-2}$	$2.209 \cdot 10^0$	OOM	$6.070 \cdot 10^{-2}$	$8.810 \cdot 10^{-2}$
DeepONet	$1.697 \cdot 10^{-3}$	$2.003 \cdot 10^{-2}$	$3.968 \cdot 10^{-2}$	$8.589 \cdot 10^{-2}$	$2.492 \cdot 10^{-1}$
Sulzer and Buck I	$1.475 \cdot 10^{-3}$	$1.970 \cdot 10^{-3}$	$2.132 \cdot 10^{-2}$	$3.633 \cdot 10^{-2}$	$5.627 \cdot 10^{-2}$
Sulzer and Buck II	$7.645 \cdot 10^{-4}$	$1.598 \cdot 10^{-3}$	$1.797 \cdot 10^{-1}$	$3.391 \cdot 10^{-2}$	$5.517 \cdot 10^{-2}$
LiLaN	$2.80 \cdot 10^{-4}$	$1.981 \cdot 10^{-3}$	$7.486 \cdot 10^{-3}$	$1.072 \cdot 10^{-2}$	$4.741 \cdot 10^{-2}$

Table 2: Wall clock time comparison of LiLaN with traditional numerical solver

Speed tests in wall clock time					
Problem	Robertson	CR charge state	Full CR model	Allen-Cahn	Cahn-Hilliard
Numerical Solver	6232.8s	11034.1s	10955.5s	53.25s	212.1s
LiLaN	7.648s	7.366s	13.604s	3.729s	15.485s
Speedup	815.0x	1498.0x	805.3x	14.3x	13.7x

5 Conclusion

In this paper, we have presented a novel, machine learning approach, called LiLaN, for fast and accurate simulation of stiff, nonlinear, ordinary and partial differential equations. LiLaN is inspired by kernel methods in which the original problem under consideration is featurized/lifted to (much) higher dimensional feature spaces where the problem is now easier. In particular, LiLaN, via nonlinear neural networks, lifts the original stiff problems into higher dimensions where the problem is no longer stiff. Unlike kernel methods which rely on particular feature maps to organize the latent dynamics so that hopefully it is easier to simulate, LiLaN forces the latent dynamics to be trivially linear, and then learns the nonlinear feature maps using neural networks—the encoders. With linear latent dynamics that admits analytical solutions, no numerical integration, but instead evaluations of encoders/decoders, are needed during the inference stage, and this is key to LiLaN’s real-time efficiency. LiLaN is thus a solution operator approach that learns the flow maps of nonlinear systems of ODEs. Indeed, theoretical results show that LiLaN can approximate an arbitrary continuous flow map to any desired accuracy and that the latent dimension is independent of the accuracy. Various numerical results with varying dimensionality, complexity, and stiffness have been presented to demonstrate the speed and accuracy of LiLaN against contemporary machine learning and numerical methods. Numerical results also show that the temporal nonlinear mapping into the latent space plays a vital role in achieving better generalization performance especially when using coarse time grids for training the networks. In particular, LiLaN architectures show better generalization capabilities compared to a direct learning method for approximating the flow map of a system of ODEs. It should be pointed out that, in this paper, though the motivation and numerical examples for LiLaN are stiff ODEs, it is equally applicable to non-stiff ODEs. Part of our future work will focus on additional theoretical analysis (non-asymptotic analysis) and numerical results to address the question of why LiLaN outperformed the direct learning approach for learning flow maps. For many problems, data generation may be costly, and part of our future work is to develop algorithms for adaptive data sampling (active learning) to reduce the amount of data required to train each model, while also answering the question of finding the optimal neural network architecture (number of layers, number of neurons in each layer) for prediction such as in [44].

6 Acknowledgments

This research is partially funded by the National Science Foundation award NSF-OAC-2212442 and by the Department of Energy awards DE-SC0024724 and DE-SC0024633. The authors would like to thank Wesley Lao and Hai Nguyen for productive conversations. The authors also acknowledge the Texas Advanced Computing Center (TACC) at The University of Texas at Austin for providing HPC resources that have been vital to the research results reported within this paper. URL: <http://www.tacc.utexas.edu>

References

- [1] Ranjan Anantharaman, Yingbo Ma, Shashi Gowda, Chris Laughman, Viral Shah, Alan Edelman, and Chris Rackauckas. Accelerating simulation of stiff nonlinear systems using continuous-time echo state networks, 2021.
- [2] H.-K Chung, M.H. Chen, W.L. Morgan, Yuri Ralchenko, and Richard Lee. Flychk: Generalized population kinetics and spectral model for rapid spectroscopic analysis for all elements. *High Energy Density Physics*, 1, 06 2005.
- [3] Hadrien Montanelli and Niall Bootland. Solving periodic semilinear stiff pdes in 1d, 2d and 3d with exponential integrators, 2020.
- [4] W.L. Miranker. *The Computational Theory of Stiff Differential Equations*. Publication mathématique d’Orsay ; no 219-7667. Université Paris XI, U.E.R. mathématique, 1976.
- [5] Mark Davis. Numerical methods & modeling for chemical engineers. 01 1984.

- [6] Peter Benner, Serkan Gugercin, and Karen Willcox. A survey of projection-based model reduction methods for parametric dynamical systems. *SIAM Review*, 57:483–531, 06 2015.
- [7] Evangelos Galaris, Gianluca Fabiani, Francesco Calabrò, Daniela di Serafino, and Constantinos Siettos. Numerical solution of stiff odes with physics-informed rpns, 2021.
- [8] Hai Van Nguyen, Jau-Uei Chen, and Tan Bui-Thanh. A model-constrained discontinuous galerkin network (dgnet) for compressible euler equations with out-of-distribution generalization. *arXiv preprint arXiv:2409.18371*, 2024.
- [9] Immanuel Sulzer and Tobias Buck. Speeding up astrochemical reaction networks with autoencoders and neural odes, 2023.
- [10] Henry Dikeman, Hongyuan Zhang, and Suo Yang. Stiffness-reduced neural ode models for data-driven reduced-order modeling of combustion chemical kinetics. 01 2022.
- [11] Ricky T. Q. Chen, Yulia Rubanova, Jesse Bettencourt, and David Duvenaud. Neural ordinary differential equations, 2019.
- [12] Hai V Nguyen and Tan Bui-Thanh. A model-constrained tangent slope learning approach for dynamical systems. *International Journal of Computational Fluid Dynamics*, 36(7):655–685, 2022.
- [13] Suyong Kim, Weiqi Ji, Sili Deng, Yingbo Ma, and Christopher Rackauckas. Stiff neural ordinary differential equations. *Chaos: An Interdisciplinary Journal of Nonlinear Science*, 31(9), September 2021.
- [14] Tadbhagya Kumar, Anuj Kumar, and Pinaki Pal. A physics-constrained neuralode approach for robust learning of stiff chemical kinetics. 12 2023.
- [15] Maziar Raissi, Paris Perdikaris, and George Em Karniadakis. Physics informed deep learning (part i): Data-driven solutions of nonlinear partial differential equations, 2017.
- [16] Sifan Wang, Yujun Teng, and Paris Perdikaris. Understanding and mitigating gradient pathologies in physics-informed neural networks, 2020.
- [17] Weiqi Ji, Weilun Qiu, Zhiyu Shi, Shaowu Pan, and Sili Deng. Stiff-pinn: Physics-informed neural network for stiff chemical kinetics. *The Journal of Physical Chemistry A*, 125(36):8098–8106, August 2021.
- [18] Hubert Baty. Solving stiff ordinary differential equations using physics informed neural networks (pinns): simple recipes to improve training of vanilla-pinns, 2023.
- [19] Pouyan Nasiri and Roozbeh Dargazany. Reduced-pinn: An integration-based physics-informed neural networks for stiff odes, 2022.
- [20] Xuping Xie, Qi Tang, and Xianzhu Tang. Latent space dynamics learning for stiff collisional-radiative models. *Machine Learning: Science and Technology*, 5(4):045070, dec 2024.
- [21] Kookjin Lee and Eric J. Parish. Parameterized neural ordinary differential equations: applications to computational physics problems. *Proceedings of the Royal Society A: Mathematical, Physical and Engineering Sciences*, 477(2253):20210162, September 2021.
- [22] Bethany Lusch, J. Nathan Kutz, and Steven L. Brunton. Deep learning for universal linear embeddings of nonlinear dynamics. *Nature Communications*, 9(1), November 2018.
- [23] Omri Azencot, N. Benjamin Erichson, Vanessa Lin, and Michael W. Mahoney. Forecasting sequential data using consistent koopman autoencoders, 2020.
- [24] Somdatta Goswami, Ameya D. Jagtap, Hessam Babae, Bryan T. Susi, and George Em Karniadakis. Learning stiff chemical kinetics using extended deep neural operators, 2023.
- [25] Elizaveta Levina and Peter J. Bickel. Maximum likelihood estimation of intrinsic dimension. In *Neural Information Processing Systems*, 2004.

- [26] Erik Bollt. On explaining the surprising success of reservoir computing forecaster of chaos? The universal machine learning dynamical system with contrast to VAR and DMD. *Chaos: An Interdisciplinary Journal of Nonlinear Science*, 31(1):013108, 01 2021.
- [27] Kei Ota, Tomoaki Oiki, Devesh K. Jha, Toshisada Mariyama, and Daniel Nikovski. Can increasing input dimensionality improve deep reinforcement learning?, 2020.
- [28] Hartmut Logemann, Eugene P Ryan, et al. *Ordinary differential equations: analysis, qualitative theory and control*. Springer, 2014.
- [29] Patrick Kidger and Terry Lyons. Universal approximation with deep narrow networks. In *Conference on learning theory*, pages 2306–2327. PMLR, 2020.
- [30] Tan Bui-Thanh. A unified and constructive framework for the universality of neural networks. *IMA Journal of Applied Mathematics*, page hxad032, 11 2023.
- [31] Midhun T Augustine. A survey on universal approximation theorems. *arXiv preprint arXiv:2407.12895*, 2024.
- [32] Ingo Gühring, Mones Raslan, and Gitta Kutyniok. Expressivity of deep neural networks, 2020.
- [33] George F Simmons. *Differential equations with applications and historical notes*. CRC Press, 2016.
- [34] Gerald Teschl. *Ordinary differential equations and dynamical systems*, volume 140. American Mathematical Society, 2024.
- [35] John M Lee. *Introduction to topological manifolds*. Springer, 2000.
- [36] Walter Rudin. Principles of mathematical analysis. 2021.
- [37] Morris W Hirsch, Stephen Smale, and Robert L Devaney. *Differential equations, dynamical systems, and an introduction to chaos*. Academic press, 2013.
- [38] Anne Kværnø. Singly diagonally implicit runge–kutta methods with an explicit first stage. *BIT Numerical Mathematics*, 44(3):489–502, 2004.
- [39] Patrick Kidger. *On Neural Differential Equations*. PhD thesis, University of Oxford, 2021.
- [40] Nathan A Garland, Romit Maulik, Qi Tang, Xian-Zhu Tang, and Prasanna Balaprakash. Efficient data acquisition and training of collisional-radiative model artificial neural network surrogates through adaptive parameter space sampling. *Machine learning: science and technology*, 3(4):045003, 2022.
- [41] E. Süli and D.F. Mayers. *An Introduction to Numerical Analysis*. An Introduction to Numerical Analysis. Cambridge University Press, 2003.
- [42] William E. Schiesser. *The Numerical Method of Lines: Integration of Partial Differential Equations*. Elsevier, 2012.
- [43] S.M. Cox and P.C. Matthews. Exponential time differencing for stiff systems. *Journal of Computational Physics*, 176(2):430–455, 2002.
- [44] CG Krishnanunni, Tan Bui-Thanh, and Clint Dawson. Topological derivative approach for deep neural network architecture adaptation. *arXiv preprint arXiv:2502.06885*, 2025.

A General setting for numerical experiments

A.1 Data Transformations

ODE Problems: sections 3.1 and 3.2

To address the multiscale nature of the data in the three ODE problems, as a preprocessing step, all time series data is

log scaled using the base 10 logarithm. This procedure reduces the scale separation of different components of the solution. As an additional training aid, all network inputs, apart from time, are scaled independently to the range $[-1, 1]$. Finally, the time discretization points are log scaled, using the base 10 logarithm, and then rescaled to fit the range $[0, 1]$ seconds. Additionally, since each of the ODE problems is conservative (Robertson ODE has conservation of total concentration and CR ODEs have conservation of total number of electrons), we implement conservation constraints implicitly, by applying a softmax to the output of the decoder and multiplying by the appropriate constant (known from \mathbf{x}_0) to obtain a solution satisfying the conservation constraint.

PDE Problems: sections 3.3 and 3.4

For both PDE models, the data all lies on the range $[-1, 1]$, so no rescaling is required. However, the time discretization points are rescaled to fit the range $[0, 1]$ seconds.

A.2 Training for Multiscale Stiff Systems

In all of the ODE (sections 3.1 and 3.2) test problems presented in this paper, the unique degrees of freedom in the solution vary by several orders of magnitude. This led to challenges in training with traditional loss functions such as mean squared error (MSE). In training, such loss functions were heavily biased toward learning the large magnitude components of the solution. To remedy this issue, we considered an absolute relative error loss function. The use of relative error balances out the magnitudes of errors for each individual degree of freedom.

$$\mathcal{L}(\mathbf{X}; \boldsymbol{\alpha}, \boldsymbol{\beta}, \boldsymbol{\nu}, \boldsymbol{\theta}) = \frac{1}{(N+1) \cdot (M+1)} \sum_{i=0}^N \sum_{j=0}^M \left| \frac{\mathbf{x}_i(t_j) - \hat{\mathbf{x}}_i(t_j)}{\mathbf{x}_i(t_j)} \right|. \quad (39)$$

where, the predicted state $\hat{\mathbf{x}}_i(t_j)$ for time t_j and for the i^{th} training input $\{(\mathbf{x}_0)_i, \mathbf{p}_i\}$ is given by (41). $\mathbf{x}_i(t_j)$ denotes the actual state at time t_j for the i^{th} input. However, this loss function still has the problem that overshooting errors are punished much more harshly than undershooting errors. Finally, we settled on the following loss function which resolves the unbalanced penalties between overshooting and undershooting.

$$\mathcal{L}(\mathbf{X}; \boldsymbol{\alpha}, \boldsymbol{\beta}, \boldsymbol{\nu}, \boldsymbol{\theta}) = \frac{1}{N+1} \sum_{i=0}^N \prod_{j=0}^M 10^{\frac{1}{M+1} |\mathbf{x}_i(t_j) - \hat{\mathbf{x}}_i(t_j)|}, \quad (40)$$

$$\hat{\mathbf{x}}_i(t_j) = \mathbf{d}(e((\mathbf{x}_0)_i, \mathbf{p}_i; \boldsymbol{\alpha}) + \boldsymbol{\tau}(t_j, (\mathbf{x}_0)_i, \mathbf{p}_i; \boldsymbol{\nu}) \circ \mathbf{c}(\mathbf{x}_{0_i}, \mathbf{p}_i; \boldsymbol{\beta}); \boldsymbol{\theta}). \quad (41)$$

In (39) and (40), \mathbf{X} is a third order tensor containing $[\mathbf{x}(t_j)]_i$ for all samples, $s = 0, \dots, N_s$, and all times, $t = 0, \dots, N_t$, in the dataset.

The above loss function is used for the ODE problems which are trained using a log scaled version of the original data. For the PDE problems (sections 3.3 and 3.4), the data is not log scaled so a different loss function was chosen. We do not use an absolute error style loss function, since some of the true data is 0, meaning the relative error will be undefined at those points. Instead, the evaluation metric (43) was used as the loss function in training.

A.3 Error Evaluation Metrics

The plots, in this paper, depicting point-wise relative error over time, report the relative error in the Euclidean norm, averaged over all N samples, given as

$$\mathcal{R}_1 = \frac{1}{N+1} \sum_{i=0}^N \frac{\|\mathbf{x}_i(t_j) - \hat{\mathbf{x}}_i(t_j)\|_2}{\|\mathbf{x}_i(t_j)\|_2}. \quad (42)$$

Table 1 reports the point-wise relative error in the Euclidean norm, averaged over all N samples and M time steps, given as:

$$\mathcal{R}_2 = \frac{1}{(N+1) \cdot (M+1)} \sum_{i=0}^N \sum_{j=0}^M \frac{\|\mathbf{x}_i(t_j) - \hat{\mathbf{x}}_i(t_j)\|_2}{\|\mathbf{x}_i(t_j)\|_2}. \quad (43)$$

A.4 Description of methods adopted for comparison

LiLaN is compared with the four approaches described below:

DeepONet : An operator learning approach with branch networks, taking the state as its input, and trunk networks, taking time as its input, with the inner product of their respective outputs being the predicted solution, as described in [24].

Neural ODE : A scheme for approximating the right hand side of a parameterized ODE with a neural network and solving using traditional numerical integration schemes, as described in [21]. The solver used with the Neural ODEs implemented in our work is an implicit Euler scheme. Data and time steps are rescaled in ways resembling the methodology in [13].

Sulzer and Buck I : A Neural ODE approach in a reduced dimension ($n_x \geq m$) latent space, described in [9], in which the right hand side is considered a constant function of the encoded initial condition.

Sulzer and Buck II : A Neural ODE approach in an expanded dimension ($n_x \leq m$) latent space, in which the right hand side is considered a constant function of the encoded initial condition. This is a modified version of the approach described in [9].

A.5 Architectural Details

Tables 3 to 7 show the neural network architectures used for each machine learning method and problem setting. Each network uses the *tanh* activation function at each hidden layer and has a linear output layer. The notation, $[*, \dots, *]$, indicates the number of neurons in each layer for a multilayer perceptron network, including the initial input layer. Recall that, since we use the independent architectural variants for testing each ODE problem, there is one network of each type per degree of freedom in the system of ODEs for LiLaN and DeepONet. Networks following the "independent" architectural variant from section 2.3 are labeled with a $*$ in the following table. All other networks are implemented as the "full" variant from section 2.3. The labels (DR1) and (DR2) denote the architectures which were used in the data reduction experiments, described in section 3.5. The label (DR1) indicates our approach, while (DR2) indicates the omission of the time transform. For problems, in the table without a (DR1) entry, the same architecture used in section 3 was used for the data reduction experiments.

A.6 Choice of Latent Dimension m for each problem

The choice of latent dimension m for each problem and for different approaches is shown in table 8.

A.7 Hyperparameter Settings

Table 9 shows the hyperparameter settings used in training for each method and problem setting. In each ODE problem, the batch size is approximately 5% of the total samples. In the PDE problems (sections 3.3 and 3.4), the entire training set is given to the network as a single batch. The label (DR) in the table indicates the hyperparameter setting used in section 3.6, which contains experiments on coarsening the time discretization of training data.

Table 3: Architecture for LiLaN for each problem.

LiLaN Approach					
Problem	Encoder e	Encoder c	Encoder τ	Decoder d	Total Parameters
Robertson*	[3,20,5]	[3,20,5]	[4,20,5], 5	[5,20,20,1]	3, 423
Robertson* (DR2)	[3,23,5]	[3,23,5]	N/A	[5,23,23,1]	3, 414
CR Charge States*	[3,20,5]	[3,20,5]	[4,20,5], 5	[5,20,20,1]	4, 564
CR Charge States* (DR2)	[3,23,5]	[3,23,5]	N/A	[5,23,23,1]	4, 552
Full CR*	[3,40,20]	[3,40,20]	[4,40,20], 20	[20,40,40,1]	518, 974
Full CR* (DR1)	[3,40,5]	[3,40,5]	[4,40,5], 5	[5,40,40,1]	287, 734
Full CR* (DR2)	[3,44,5]	[3,44,5]	N/A	[5,44,44,1]	290, 554
Allen-Cahn	[201,201,201]	[201,201,201]	[202,201,201], 201	[201,201,201,201]	365, 820
Allen-Cahn (DR1)	[201,100,20]	[201,100,20]	[202,100,20], 20	[20,100,100,201]	99, 281
Allen-Cahn (DR2)	[201,155,20]	[201,155,20]	N/A	[202,155,155,20]	99, 596
Cahn-Hilliard	[201,201,201]	[201,201,201]	[202,201,201], 201	[201,201,201,201]	365, 820
Cahn-Hilliard (DR1)	[201,100,20]	[201,100,20]	[20,100,201], 20	[20,100,100,201]	99, 281
Cahn-Hilliard (DR2)	[201,155,20]	[201,155,20]	N/A	[20,155,155,201]	99, 596

Table 4: Architecture for Sulzer and Buck I for each problem.

Sulzer and Buck I				
Problem	Encoder	Neural ODE	Decoder	Total Parameters
Robertson	[3,49,3]	[3,49,3]	[3,49,49,3]	3, 488
CR Charge States	[3,55,4]	[4,55,4]	[4,55,55,4]	4, 522
Full CR	[3,645,16]	[16,645,16]	[16,645,645,94]	522, 576
Allen-Cahn	[201,390,34]	[34,390,34]	[34,390,390,201]	363, 749
Cahn-Hilliard	[201,390,34]	[34,390,34]	[34,390,390,201]	363, 749

Table 5: Architecture for Sulzer and Buck II for each problem.

Sulzer and Buck II				
Problem	Encoder	Neural ODE	Decoder	Total Parameters
Robertson	[3,33,15]	[15,33,15]	[15,33,33,3]	3, 432
CR Charge States	[3,36,20]	[20,36,20]	[20,36,36,4]	4, 616
Full CR	[3,67,1880]	[1880,67,1880]	[1880,67,67,94]	518, 950
Allen-Cahn	[201,250,201]	[201,250,201]	[201,250,250,201]	365, 603
Cahn-Hilliard	[201,250,201]	[201,250,201]	[201,250,250,201]	365, 603

Table 6: Architecture for DeepONet for each problem.

DeepONet			
Problem	Branch Network	Trunk Network	Total Parameters
Robertson	[3,20,20,5]	[1,20,20,5]	3, 510
CR Charge States	[3,20,20,5]	[1,20,20,5]	4, 680
Full CR	[3,42,42,20]	[1,42,42,20]	524, 896
Allen-Cahn	[201,8,8,8]	[1,8,8,8]	356, 976
Cahn-Hilliard	[201,8,8,8]	[1,8,8,8]	356, 976

Table 7: Architecture for Neural ODE for each problem.

Neural ODE		
Problem	Network	Total Parameters
Robertson	[6,39,39,39,3]	3, 513
CR Charge States	[7,45,45,45,4]	4, 684
Allen-Cahn	[201,338,338,338,201]	365, 579
Cahn-Hilliard	[201,338,338,338,201]	365, 579

Table 8: Latent dimension m for each problem.

	LiLaN	Sulzer and Buck I	Sulzer and Buck II	DeepONet
Robertson	15	3	15	15
CR Charge States	20	4	20	20
Full CR	1880	16	1880	1880
Allen-Cahn	201	34	201	201
Cahn-Hilliard	201	34	201	201

Table 9: Hyperparameter settings for each problem.

Training Hyperparameter Settings				
Problem	Learning Rate	Training Samples	Batch Size	Training epochs
Robertson	10^{-5}	4, 096	204	10, 000
Robertson (DR)	10^{-5}	128	6	10, 000
CR Charge States	10^{-4}	15, 625	781	10, 000
CR Charge States (DR)	10^{-4}	125	6	10, 000
Full CR	10^{-4}	4, 096	204	10, 000
Full CR (DR)	10^{-4}	256	12	10, 000
Allen-Cahn	10^{-4}	900	900	20, 000
Allen-Cahn (DR)	10^{-4}	900	900	50, 000
Cahn-Hilliard	10^{-4}	900	900	20, 000
Cahn-Hilliard (DR)	10^{-4}	900	900	100, 000

A.8 Initialization Sensitivity Studies

A.8.1 Robertson Chemical Reaction ODE

For the Robertson ODE (section 3.1), we trained networks considering 100 random parameter initializations. In figure 23, the left plot shows the mean relative error over time (42) on a test dataset of 512 samples, while the right plot shows the width of the error band over time. The width of the error band generally stays on the same scale as the error.

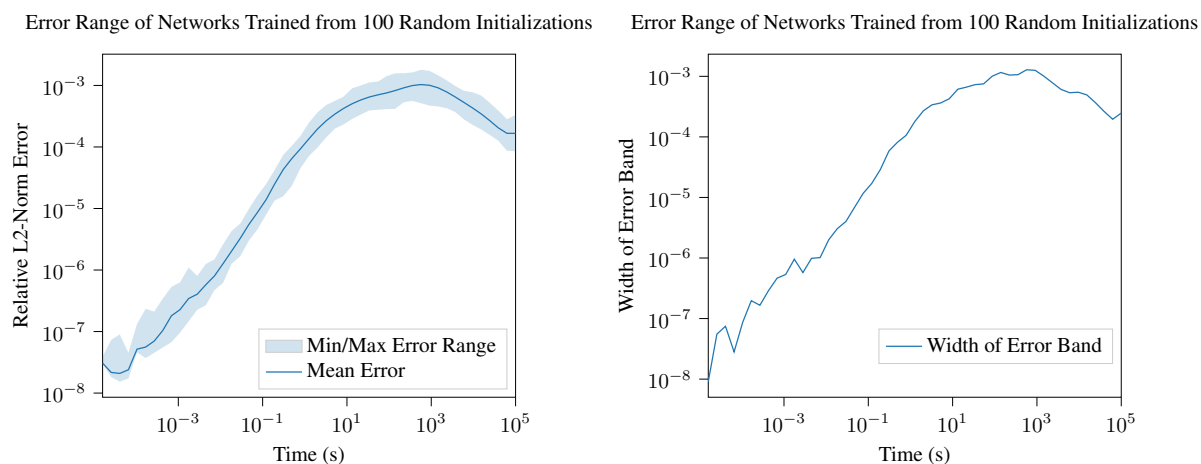


Figure 23: Left to Right: Mean relative error for Robertson ODE (section 3.1) test dataset, calculated by (42), across 100 random network parameter initializations, with min-max range; Maximum - Minimum error band width over time

A.8.2 Collisional-Radiative Model

For the CR charge state model (section 3.2), we, again, trained networks from 100 random parameter initializations. In figure 24, the left plot shows the mean relative error over time (42) on a test dataset of 4096 samples, while the right plot shows the width of the error band over time. The width of the error band generally stays on the same scale as the error.

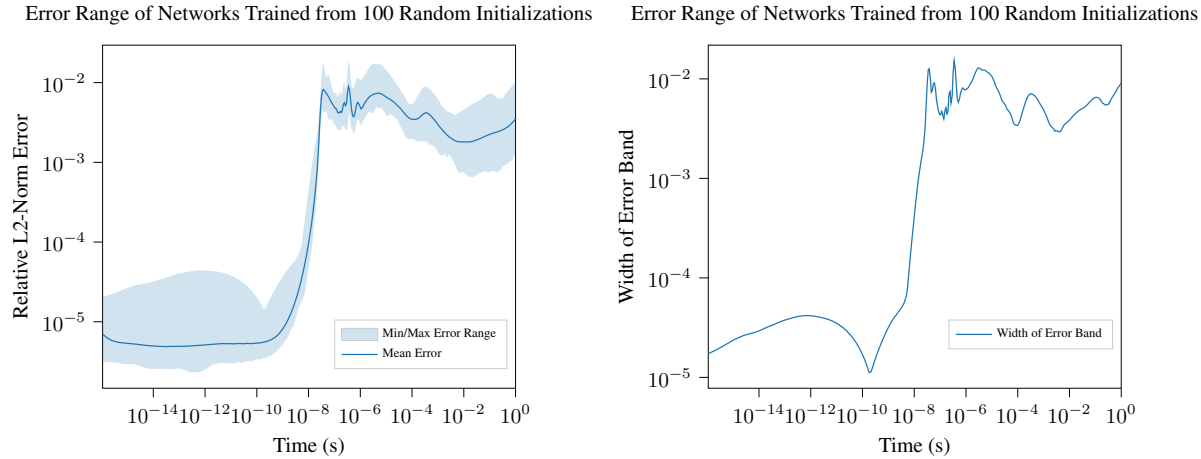


Figure 24: Left to Right: Mean relative error for CR charge state model (section 3.2) test dataset, calculated by (42), across 100 random network parameter initializations, with min-max range; Maximum - Minimum error band width over time

For the full CR model (section 3.2), we trained networks from 15 random parameter initializations. Fewer networks were trained because the networks are much more costly to train on this problem. In figure 25, the left plot shows the mean relative error over time (42) on a test dataset of 2500 samples, while the right plot shows the width of the error band over time. The width of the error band generally stays on the same scale as the error.

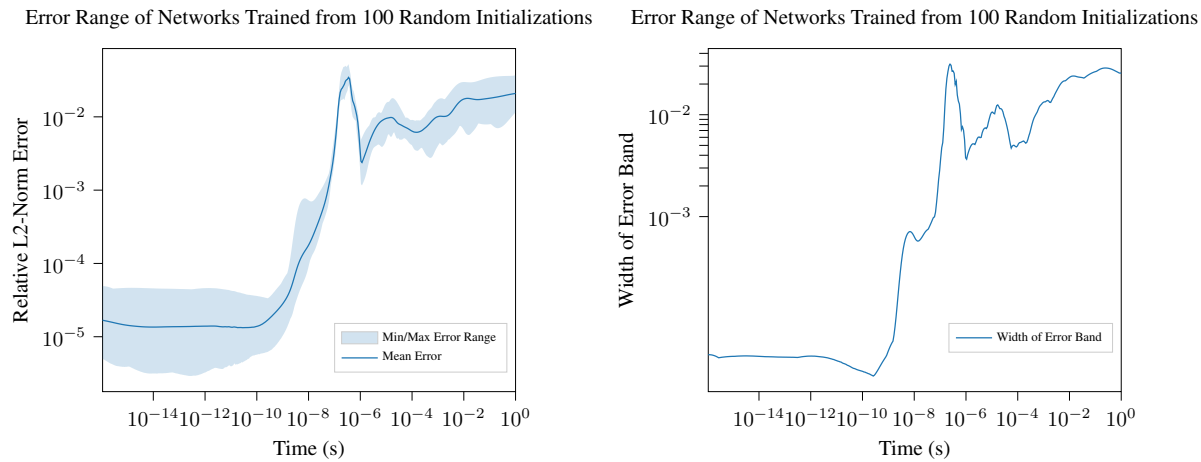


Figure 25: Left to Right: Mean relative error for full CR model (section 3.2) test dataset, calculated by (42), across 100 random network parameter initializations, with min-max range; Maximum - Minimum error band width over time

A.8.3 Allen-Cahn PDE

For the Allen-Cahn PDE (section 3.3), we trained networks from 100 random parameter initializations. In figure 26, the left plot shows the mean relative error over time (42) on a test dataset of 200 samples, while the right plot shows the width of the error band over time. The width of the error band generally stays on the same scale as the error.

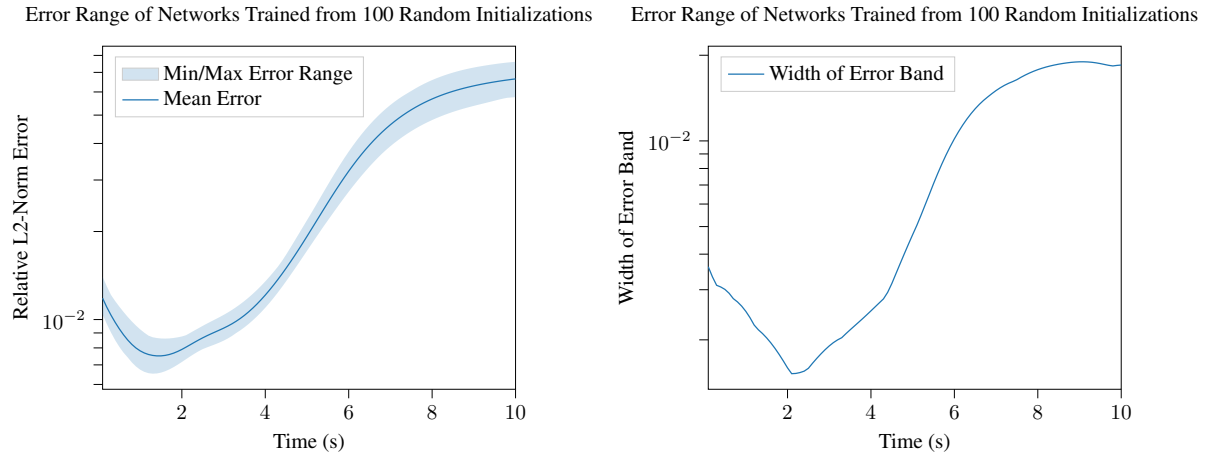


Figure 26: Left to Right: Mean relative error for Allen-Cahn (section 3.3) test dataset, calculated by (42), across 100 random network parameter initializations, with min-max range; Maximum - Minimum error band width over time

A.8.4 Cahn-Hilliard PDE

For the Cahn-Hilliard PDE (section 3.4), we trained networks from 100 random parameter initializations. In figure 27, the left plot shows the mean relative error over time (42) on a test dataset of 200 samples, while the right plot shows the width of the error band over time. The width of the error band generally stays on the same scale as the error.

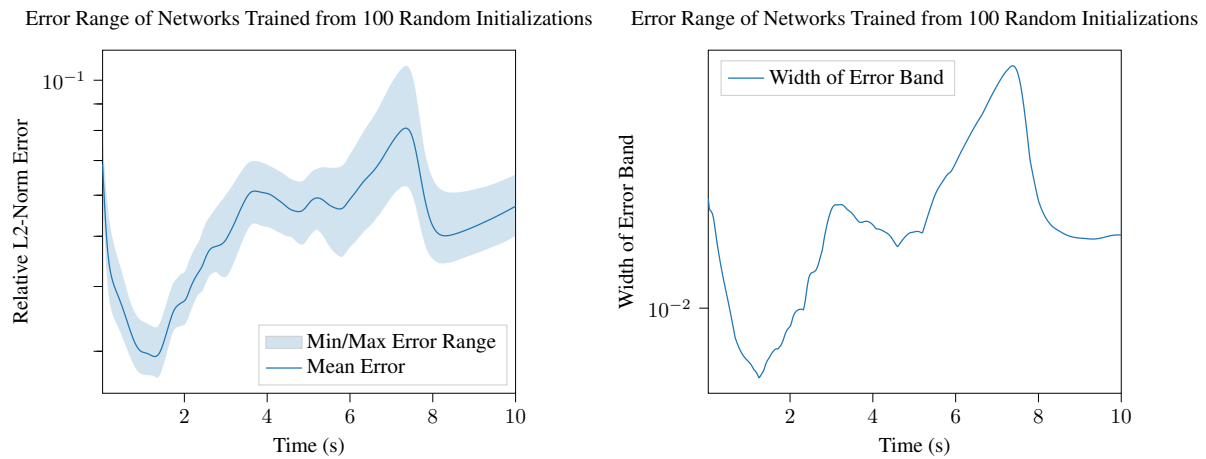


Figure 27: Left to Right: Mean relative error for Cahn-Hilliard (section 3.4) test dataset, calculated by (42), across 100 random network parameter initializations, with min-max range; Maximum - Minimum error band width over time